Published in final edited form as:
Meteorit Planet Sci. 2020 February 1; 55(2): 326–351. doi:10.1111/maps.13420.

Hydrogen fluence in Genesis collectors: Implications for acceleration of solar wind and for solar metallicity

Gary R. HUSS[1,*], **Elizabeth KOEMAN-SHIELDS**[1], **Amy J. G. JUREWICZ**[2], **Donald S. BURNETT**[3], **Kazuhide NAGASHIMA**[1], **Ryan OGLIORE**[4], **Chad T. OLINGER**[5]

[1]Hawai'i Institute of Geophysics and Planetology, University of Hawai'i at Mānoa, 1680 East-West Road, POST 504, Honolulu, Hawai'i 96822, USA

[2]Center for Meteorite Studies, Arizona State University, 781 E. Terrace Rd, ISTB4-m/c 6004, Tempe, Arizona 85287-6004, USA

[3]Division of Geological and Planetary Science, California Institute of Technology, Mail Code 100-23, 1200 E. California Blvd., Pasadena, California 91125, USA

[4]Department of Physics, Washington University in St. Louis, One Brookings Drive, St. Louis, Missouri 63130, USA

[5]GET-NSA, LLC, AU-62, 19901 Germantown Rd, Germantown, Maryland 20875, USA

Abstract

NASA's Genesis mission was flown to capture samples of the solar wind and return them to the Earth for measurement. The purpose of the mission was to determine the chemical and isotopic composition of the Sun with significantly better precision than known before. Abundance data are now available for noble gases, magnesium, sodium, calcium, potassium, aluminum, chromium, iron, and other elements. Here, we report abundance data for hydrogen in four solar wind regimes collected by the Genesis mission (bulk solar wind, interstream low-energy wind, coronal hole high-energy wind, and coronal mass ejections). The mission was not designed to collect hydrogen, and in order to measure it, we had to overcome a variety of technical problems, as described herein. The relative hydrogen fluences among the four regimes should be accurate to better than ±5–6%, and the absolute fluences should be accurate to ±10%. We use the data to investigate elemental fractionations due to the first ionization potential during acceleration of the solar wind. We also use our data, combined with regime data for neon and argon, to estimate the solar neon and argon abundances, elements that cannot be measured spectroscopically in the solar photosphere.

[*]Corresponding author. ghuss@higp.hawaii.edu.

Editorial Handling—Dr. Marc Caffee

SUPPORTING INFORMATION
Additional supporting information may be found in the online version of this article.

INTRODUCTION

The Genesis mission was flown to collect solar matter in the form of solar wind using high-purity collectors and returned it to the Earth for analysis. The overall science objectives were to (1) obtain solar isotopic abundances to the level of precision required for the interpretation of planetary science data, (2) significantly improve knowledge of solar elemental abundances, (3) measure the composition of different solar wind regimes, and (4) provide a reservoir of solar matter to serve the needs of planetary science in the 21st century (Burnett et al. 2003). The spacecraft was launched in 2001, and the samples were returned in 2004, after 853 days of exposure outside of the Earth's magnetosphere at the L1 point. Many instruments for collecting solar wind were flown (Burnett 2013). However, the samples used for this work came from the collector array, which consisted of four arrays designed to collect different energy regimes (and thereby different sources) of solar wind. The regimes were bulk solar wind (B/C array), the low-energy interstream wind (L array), high-energy coronal hole wind (H array), and coronal mass ejections (E array). Two other instruments aboard the spacecraft, the ion and electron electrostatic analyzers, monitored the solar wind energy and charge state and their data were used to trigger the deployment of the correct array for each solar wind regime. In addition, as they recorded the flow of solar wind components, they provided an independent estimate of the hydrogen flux.

The return of the Genesis spacecraft to the Earth was traumatic. A fabrication error caused the parachute not to deploy, so the spacecraft crashed into the Utah desert. Most of the collector materials were broken into small pieces, and they were dusted with Utah dirt and spacecraft debris. Luckily, the solar wind is trapped *inside* the collectors and is isolated from the contamination. The collector fragments were recovered, cleaned, and new techniques have been developed to analyze them. A sample of the solar wind is here on the Earth, and we are working hard to measure it.

Since the return of the Genesis spacecraft in 2004, several of the original mission objectives have been completed. Examples include: high-precision measurements of noble gases in bulk solar wind and the regimes have been obtained (Heber et al. 2009a, 2009b, 2011, 2012; Meshik et al. 2014), determination of the oxygen isotopic composition of the Sun (McKeegan et al. 2011), and determination of the nitrogen isotopic composition of the Sun (Marty et al. 2011; Huss et al. 2012). In addition, the abundances of several other elements in the solar wind have been obtained: magnesium and iron (Jurewicz et al. 2011); potassium and sodium (Rieck et al. 2016); calcium, aluminum, and chromium (Heber et al. 2014). A study of the magnesium isotopic composition of the solar wind is presented in Jurewicz et al. (2020). More detailed reviews of past, current, and future Genesis studies can be found in Burnett (2013) and in Burnett et al. (2019).

Measuring the hydrogen fluence of the solar wind was not one of the initial mission objectives. However, as we worked with the collectors, it seemed that measuring the hydrogen fluence should be relatively straightforward using secondary ion mass spectrometry (SIMS; also known as the ion microprobe). Moreover, it seemed to be a useful thing to do. An accurate and precise measurement of the hydrogen accompanying the other elements in the solar wind would enable the evaluation of models of elemental and isotopic

fractionation during acceleration of the solar wind. For example, elements are fractionated according to their first ionization potential (FIP) during solar wind acceleration (e.g., Bochsler 2000, 2007a; Laming et al. 2017). Elements with low FIP are easily ionized in the chromosphere and are more efficiently transported upward to the corona than high-FIP elements. The transition in FIP-controlled fractionation is at ~10 eV in the solar energetic particles, but is at ~14 eV in the solar wind. Hydrogen, with a FIP of 13.6 eV, lies in this range and could provide important information about elemental fractionations in the solar wind (e.g., Reames 2018).

A sample-based H fluence could also permit an independent estimate of the metallicity of the Sun (the mass fraction of elements other than hydrogen and helium), a quantity that has a fundamental importance in determining the past and future evolution of the Sun. With the introduction of 3D modeling of the solar photosphere, the inferred metallicity of the Sun dropped by 30–40% (e.g., Asplund et al. 2009). However, the older higher metallicity agreed well with the requirements of models of solar structure from helioseismology, while the new lower metallicity is inconsistent with those (Basu and Antia 2004, 2008). There have been several proposals that attempt to reconcile this inconsistency (e.g., Bahcall et al. 2005; von Steiger and Zurbuchen 2016), but to date the inconsistency has not been resolved. The hydrogen fluence value obtained in this study may help address this issue.

Measuring solar wind hydrogen in the Genesis collectors did turn out to be relatively easy. However, converting the measurements into robust estimates of solar wind fluences has been quite challenging. We had to account for variations in relative sensitivity of hydrogen with respect to many different measurement parameters in the ion microprobe (see below), and standardization turned out to be very challenging. We eventually resolved most of these problems. Accordingly, presented here are our measurements of the hydrogen fluence in the bulk solar wind collector (B/C array) and in the L-, H-, and E-array collectors. We also discuss some first-order interpretations that can be made from these results.

SAMPLES AND EXPERIMENTAL METHODS

Samples and Standards

Samples and standards are summarized in Table 1. Four relatively large diamond-like-carbon-on-silicon (DOS) collectors from the Genesis Mission were allocated to this work: #60628 from the B/C bulk solar wind array, #60631 from the high-speed (coronal hole) H array, #60431 from the low-speed (interstream) L array, and #60625 from the coronal-mass-ejection E array. DOS was chosen over silicon because hydrogen diffuses much more slowly in DOS. In fact, Genesis DOS is nominally anhydrous, but hydrated versions exist, so solar wind hydrogen may be incorporated into the DOS structure and stabilized. Because there are elemental and isotopic fractionations associated with the edges of samples in ion probe measurements, the pieces were all at least 5 mm across in their smallest dimension so that they could fit behind the mask on a standard Cameca ion microprobe holder with 6 mm holes (Fig. 1). Standard materials included two terrestrial apatite crystals with known water content and a sample of flight-spare DOS material, all of which were implanted with a “known” amount of hydrogen (see below).

Measuring Solar Wind Hydrogen

The Genesis collectors were measured by ion microprobe in depth-profiling mode using the Cameca ims 1280 ion microprobe at the University of Hawai'i at Mānoa. A focused Cs^+ primary ion beam of 300–500 picoamps (pA) was used to generate negative secondary ions. Several sets of operating parameters and sample mounting strategies were investigated before we settled on the final measurement conditions. Rather than describing each of these experiments, we will summarize what we learned from them. Then, we will describe the parameters we used in detail.

Experimental Difficulties and their Solutions

Interrelationship of Sputter Rate, Beam Current, Raster Size, and Measurement Time: The sputter rate must be selected such that a measurement adequately samples the solar wind profile as a function of depth while keeping the signal strength appropriate for the chosen detector and the run time short enough so that instrument instabilities do not compromise the results. Faraday cups with feedback resisters of 10^{10}–10^{11} ohms are very stable detectors, but they work well only with signals of between a few $\times 10^6$ and a few $\times 10^9$ cps. Solar wind hydrogen is relatively abundant in the collectors, so it is not difficult to generate signals with count rates in this range. However, with negative secondary ions, the signal from carbon in the diamond-like carbon substrate, which is needed to normalize the solar wind profile, is a factor of nearly 100 higher than that for hydrogen. That leaves a relatively small range of hydrogen count rates ($[1–4] \times 10^7$ cps) over which both the hydrogen and carbon signals can be measured using Faraday cups. Measuring with Faraday cups necessitates a primary beam current of 20–30 nanoamps (nA) (a very large primary beam current for our ims 1280), which sputters the sample rapidly and does not allow for precise sampling of the solar wind implanted profile. In order to slow down the rate at which the ion beam sputters through the solar wind profile, the raster area must be increased. But there is a maximum raster size from which secondary ions can be extracted into the mass spectrometer. The practical limit is about 100 μm × 100 μm. With this raster size and a beam current of 20–30 nA, the ion probe sputters through the solar wind profile in only a few minutes, not long enough to adequately sample the shape of the profile.

We also have electron-multiplier detectors. These operate in a range of <1 to a few $\times 10^5$ cps (sometimes this can be pushed to ~10^6 cps). A hydrogen count rate of $(1–4) \times 10^5$ cps, ~100 times lower than can be measured comfortably on a Faraday cup, works well, which implies a beam current of 0.2–0.3 nA. At this beam current, the carbon count rate is still high enough for the Faraday cup, but the sputter rate from a 100 μm × 100 μm rastered area is such that measurements take many hours. The solar wind profile is very well sampled. Decreasing the raster size shortens the measurement, but if the measurement is too short, the profile will not be sampled with sufficient depth resolution.

The protocol described below was arrived at after considerable work evaluating these and other trade-offs. The individual measurements are quite long, particularly those that have the solar wind and standard profiles implanted on top of each other (see below). One of the most difficult parts of this work was to keep the ion probe primary ion current stable over the course of measurements that took as much as 9 h.

Edge Effects: Changes in the extraction field that pulls the sputtered ions into the mass spectrometer can shift the relative ion yields of sputtered species. Hydrogen in DOS is particularly subject to this problem because of its low mass to charge ratio. To evaluate the extent of ion-yield variation in DOS, we measured $^{1}H^{-}$, $^{12}C^{-}$, $^{12}C^{1}H^{-}$, and $^{12}C_{2}^{-}$ on several DOS standards mounted in several different kinds of sample holder. We found that within ~1.5 mm of an edge (edge of the sample, edge produced by the mask on the holder, etc.), the $^{1}H/^{12}C$ and $^{12}C^{1}H/^{12}C_{2}$ ratios change significantly and anticorrelate with one another. Figure 2 shows the $^{1}H/^{12}C$ and $^{12}C^{1}H/^{12}C_{2}$ ratios as a function of distance from the edge of the sample holder for one of our hydrogen standards. The behavior is reproducible and a factor (an asymmetrically weighted mean) can be calculated that converts the measured ratios into a single value for small to moderate shifts in ion yield (Fig. 2). We use a similar strategy for hydrogen in oxygen-rich compounds by measuring $^{1}H/^{16}O$ and $^{16}O^{1}H/O_{2}$. We did our best to collect data far from edges under conditions where $^{1}H/^{12}C$ and $^{12}C^{1}H/^{12}C_{2}$ ion ratios did not vary, and for the most part, we were successful. No explicit corrections for shifts in ion yield were made.

In order to get around this and other problems, we have developed a backside profiling method in which the sample is mounted in a 1 inch diameter disk and ground down from the back side to a few microns in thickness (e.g., Westphal et al. 2014). The sample is then carbon coated and the disk is mounted in a standard ion probe holder. The sample and holder present a flat, featureless surface so that the field lines are not distorted. Our backside profiling method works best for silicon wafers, which have uniform physical properties. For DOS, the silicon backing must be removed, and grinding can cause the highly stressed diamond-like carbon to fall apart. K. Rieck worked with I. Veryovkin to develop a method to completely remove the silicon from DOS wafers gently, by etching with XeF_{2} (Rieck 2015). Unfortunately, these backside profiling methods for DOS were not sufficiently well developed to use in this work.

Changes in Integrated H/C Ratio as a Function of Beam Current: We quickly learned that the integrated H/C ratio, no matter how one calculates it, depends on the primary beam current. This is because the secondary ion count rate for any element does not increase linearly with primary beam current, and different elements have different dependences on primary beam current.

Figure 3 shows the effect of changing the beam current on the integrated H/C ratio. In this case, the plotted values are the weighted means of the integrated $^{1}H/^{12}C$ and $^{12}C^{1}H/^{12}C_{2}$ ratios for one of our DOS implant standards. Increasing the beam current from 1 to 4 nA increases the value for the integrated peak by ~30%. Clearly, in order to get a consistent set of results for the Genesis BC, H, L, and E arrays, measurements must be made at as close as possible to the same primary beam current. However, beam current varies during the course of the measurement by ~3% to 8%. There are two effects of changing beam current on depth profiles. The first is the change in ionization efficiency as a function of beam current. The second is the change in sputter rate with beam current. If the beam current is changing, and an average beam current is used to determine the depth scale for the measurement, the profile will be distorted and the integrated profile will be affected. For conductive samples such as DOS, we were able to monitor the beam current during a measurement, and we

made a correction for the changing sputter rate due to a change in beam current. However, this was not possible for nonconductive samples that required the electron gun (e.g., apatite, see below) because the electron cloud produced by the electron gun affects the Faraday cup that reads the primary beam current. We did not attempt to correct for changes in sensitivity with beam current during a given run in this work as these changes are small. Note that so long as standard and solar wind are measured at the same beam current, it does not matter what the nominal beam current is. Small differences in sensitivity due to drift in beam current between standard and solar wind for internally standardized measurements and between solar wind and standard measurements in externally standardized measurements are one (relatively minor) factor in our quoted uncertainties.

Standardization: Standardization proved to be a major problem. The strategy for standardizing our Genesis depth profiles was a modification of that described in Burnett et al. (2015). Hydrogen was implanted into the Genesis chips at a level deeper than the solar wind (internal standardization), into a clean flight-spare DOS sample (external standardization), and into two apatite grains with known hydrogen content, which were used to calibrate the implant. The standards were used to determine the relative sensitivity factor (RSF) necessary to convert hydrogen counts measured in the ion probe into a hydrogen fluence for the solar wind.

Prior to putting apatite grains into the implant alongside Genesis samples and flight-spare DOS, other hydrogen implants were used. But obtaining well-calibrated implants was quite difficult. Nominal fluences reported for implantation come from current measurements, and there are often other species implanted with the isotope of choice. Over the course of this study, we evaluated five independent hydrogen implants for use as standards. However, the RSFs determined from these standards differed by several tens of percent, too much if the goal is a fluence number accurate to better than ±5%. The eventual solution was to add apatite grains to the implant in order to calibrate the implant in a kind of reverse-isotope-dilution experiment. The hydrogen in the mineral provides a constant signal of known abundance, from which an RSF for the apatite can be determined. That RSF is then used to determine the fluence of the standard implant, which in turn gives the RSF for the DOS that is used to determine the solar wind fluence. The main uncertainties in this approach are how accurately the implant profile can be integrated and how well we know the intrinsic hydrogen content of the mineral.

For this study, we chose two different apatite grains, one from the Crystal Lode pegmatite mine in Colorado and one from Lake Baikal, Sludyanka, Russia, that had previously been characterized for their hydrogen contents (reported as H_2O) by McCubbin et al. (2012). Figure 4 shows the results obtained during a single set of measurements from our main standard mounts from the two standards. These two apatite grains give the same sensitivity factor to within ±2.4%. This uncertainty appears to be due to small errors in the reported water contents of the apatite grains in McCubbin et al. (2012). For this study, we used different grains of the same materials, obtained from Dr. McCubbin for our Genesis work. We found a slightly larger difference between the sensitivity factors determined for the two standards (±5%). We currently have no way to determine which sensitivity factor is to be

preferred, so we use the mean of the two values from the grains used for our experiment to determine the solar wind hydrogen fluence, and we propagate a ±5% uncertainty.

Preparation of Standards and Samples for Measurement—To prepare our final suite of samples for the H fluence measurements, we mounted the following materials on a 3 inch × 3 inch aluminum plate: the Crystal Lode and Lake Baikal apatite, mounted in indium within an aluminum disk, samples of flight-spare DOS, and our Genesis DOS samples from the B/C and H arrays (Fig. 5). Some pieces of flight-like silicon were also included on the plate. The aluminum plate and its contents were then irradiated at Leonard Kroko, Inc. of Tustin, California, with a nominal dose of 6×10^{15} hydrogen atoms. The implant energy (30 keV) was chosen to place the implanted hydrogen well below the solar wind implants in the B/C and H arrays. We did not irradiate our samples of the L and E arrays. These were measured by comparison to implants into the flight-spare DOS pieces and to the implants into the B/C and H arrays (see below).

In retrospect, it was a mistake not to irradiate the L and E arrays with the standard implant. As described below, we found that the hydrogen ion yields (RSFs) of the various DOS chips were different. This led to different calculated fluences depending on which DOS chip was used to standardize the measurement. This property of DOS may partially explain some of the variability among our test ion implants described above. We discuss this issue in detail below.

Final Experimental Protocol—An important consideration in making hydrogen measurements is the hydrogen background in the ion probe and the amount of water adsorbed on the sample surface. For these measurements, the samples were put into the airlock several days before the measurements were to be made to minimize the amount of adsorbed water. To lower the hydrogen background in the sample chamber, the titanium sublimation pump was activated several times. The pressure in the sample chamber for the apatite measurements was $(5–6) \times 10^{-10}$ torr and for the DOS measurements was $\sim 4 \times 10^{-10}$ torr.

Two sets of analytical protocols were required to make these measurements, one for the implanted apatite grains and one for the DOS collectors and standard.

Apatite Grains: A Cs^+ primary beam of ~500 pA, focused to ~10 μm, was accelerated to +10 keV. The measurements were made in depth-profiling mode with the primary beam rastered over a $50 \times 50\ \mu m^2$ area. The electron flood gun (Egun) was used for charge compensation. The secondary-ion mass spectrometer was operated at −10 keV, giving a primary-beam impact energy of 20 keV. The data were collected in a combined multicollection and peak-jumping mode. Specifically, hydrogen was collected on the L2 electron multiplier, followed by peak jumps that put $^{16}O^-$, $^{16}O^1H^-$, $^{31}P^-$, and $^{16}O_2{}^-$ on the monocollector detectors. ^{16}O and ^{31}P were measured on Faraday cup FC2 equipped with a 10^{11}-ohm resister, and $^{16}O^1H^-$ and $^{16}O_2{}^-$ were measured on the monocollector electron multiplier. The mass resolving power for the L2 electron multiplier was ~2000 (multicollector exit slit #1). The low mass resolving power was used because there are no interferences for ^1H and because a wide-open exit slit gives a wide peak top, reducing the

need for very precise control of the magnetic field position for hydrogen. The monocollector was operated at a mass resolving power of ~5500, sufficient to resolve $^{16}O^{1}H^{-}$ from $^{17}O^{-}$ and all significant interferences on the other measured species.

To reduce the signal from unwanted hydrogen diffusing along the sample surface, an electronic gate was used to eliminate the signal from the outer part of the rastered crater; the central 36% of the rastered area was measured. To reduce the signal from the ambient gas in the sample chamber ionized by the Egun, we used a field aperture corresponding to ~37 μm on the sample surface and the dynamic transfer system. The dynamic transfer system centers the secondary ion beam generated by the primary beam from anywhere in the rastered area in the field aperture, but ions generated at random times above the sample by the primary ion beam and electron gun and those generated by the electron gun on the sample surface are partly blocked by the field aperture. Together, these strategies reduced the signal from unwanted hydrogen by ~50%. In addition, prior to each measurement, the electron gun was used to remove hydrogen from the sample surface. Normally, the electrons from the Egun arrive at the sample surface with near-zero energy. We applied an offset of ~8 eV to the sample surface, which accelerates the electrons toward the sample surface, dislodging adsorbed hydrogen. This Egun cleaning reduced the beam-off hydrogen count rate from several thousand counts per second to 30–40 counts per second. However, the surface hydrogen returns quickly, so the ion beam raster was started immediately upon stopping the electron-gun cleaning. A 500 s presputter at 500 pA (50 × 50 μm^2) was then used to further reduce the contaminant hydrogen in the measurement area. This pre-sputtering was possible because we took care to implant the hydrogen deep enough into the apatite so that the implanted hydrogen was not near the sample surface.

Each measurement on the implanted apatite standards consisted of ~300 to 500 cycles through the masses. Each cycle took ~40 s, so the total measurement lasted 3.3–5.5 h. Peak centering was checked every 50 cycles. The beam current was recorded at the beginning and end of each measurement and the variation was <~6%. The signals from $^{16}O^{-}$ and $^{16}O_2^{-}$ also provided a monitor of primary beam stability.

At the end of the measurement, the primary ion beam was turned off and an additional 50 cycles were collected to measure the hydrogen count rate generated from the volume above the sample by the electron gun. The count rate typically rose for the first few cycles before reaching a steady-state value of ~40 to ~110 counts per second. This background was subtracted before further processing was done.

B/C- and H-Array Samples: These samples were measured with Cs^{+} beam of ~300 pA. The other conditions for the primary and secondary columns were the same as those described above for the apatite standards, except as noted. For these measurements, we measured ^{1}H on the L2 electron multiplier, $^{12}C^{1}H$ on the monocollector electron multiplier, and ^{12}C and $^{12}C_2$ on monocollector Faraday cup FC2.

Because DOS is a semiconductor, we did not use the Egun during the measurements. We did use the Egun with a ~8 eV offset to reduce the surface hydrogen prior to measurement. When the electron gun was turned on with an 8 eV offset, the H count rate ranged from 10^4

to 10^5 counts per second. But after 10 min, the hydrogen count rate was below 100 counts per second with the 8 eV offset and almost undetectable with no offset. The measurement was started immediately after turning off the Egun; there was no ion-beam presputter. Measurement consisted of 700–800 cycles and lasted 8–9 h. The measurements were sufficiently long to get a flat baseline below the standard implant. We used beam-current monitoring during these measurements to track variation in the primary ion beam intensity (this was not possible for the apatite grains because the Egun affected the Faraday cup that measures the beam current).

L- and E-Array Samples and the DOS Implant: The L- and E-array samples and the standard DOS implant were all measured using a 300 pA primary Cs^+ ion beam. The conditions were the same as those for the B/C- and H-array collector measurements, including the Egun cleaning step. The measurements for the L- and E-array samples were shorter than those for the B/C- and H-array samples because there was no standard hydrogen implant below the solar wind implant. L-array measurements were 300–330 cycles (~3.5 h), while measurements for the E array, which has a deeper solar wind implant, were 500–600 cycles (5.5–6.5 h). The standard implant into the flight-spare DOS was the same as that in the B/C and H arrays, so the DOS measurements also took 750–800 cycles (~8.5 h).

Pit Documentation and Depth Determinations—Following the SIMS analyses, all analysis pits were imaged in the scanning electron microscope to identify any irregularities that might have affected the depth profile measurements. The pit depths are essential to the data reduction when using an external standard. Pit depths were measured using two independent techniques, in order to mitigate the effect of any systematic measurement errors.

The first depth measurement technique was stylus profilometry. We used the KLA Tencor AS200 instrument in the SIMS laboratory at ASU. Step height standards (either ±5% or ±1%, depending on the height of interest) were measured periodically throughout each session to make sure that the calibration was consistent. In addition, during a previous study, this instrument had participated in a “round robin” with a similar instrument at NIST, and was able to duplicate measurements of depths of SIMS pit in size range used in this study to within ~1% error.

The second depth measurement technique was optical interferometry. We used the MicroXAM instrument in Thayer School of Engineering at Dartmouth College. Interferometry can give a three-dimensional view of the analysis pit, in contrast to the linear measurements from stylus profilometry and no contact with the sample is required. Unfortunately, interferometry can be influenced by differences in composition (e.g., bottom of pit versus surface of sample). However, in the cases of both the apatite calibration standards and the DOS samples, there was no systematic difference between the pit depths measured by interferometry from those measured by stylus profilometry. For an individual measurement, depth differences between the two techniques of >1% generally reflected surface roughness.

Data Reduction

As described previously, for the solar wind collectors and flight-spare DOS standard, we collected data for H^- and CH^-, two forms of the element of interest, and for C^- and C_2^-, the dominant atomic and molecular ions from the collector. For the apatite standards, we measured H^- and OH^- along with O^-, P^-, O_2^-. Our normal data reduction protocol uses ratios (e.g., H/C, CH/C_2). The expectation is that the denominator of the ratio, which comes from the main constituent in the sample, will provide a stable reference that helps us account for changes in primary beam current and other instrument-related effects. The assumption is that the numerator and denominator in the ratios will covary with beam current, etc. But if this is not true, and the numerator and denominator vary in different ways, this introduces artifacts into the final data. We followed the normal procedure and reduced the data as ratios, but we also reduced the data as counts per second per nanoAmp (cps/nA) for H and CH. The latter data reduction helped us to sort out some issues with the DOS collectors (discussed below).

Data Reduction Using Ratios—The three sets of data (apatite, B/C- and H-array samples, and L- and E-array samples and the DOS external standard) were collected under different measurement protocols, so each had to be reduced using a different procedure. Below, we will first discuss the steps in the data reduction common to all three methods. Discussions of the distinctive parts of the data reduction for the three types of samples will follow.

Components Common to All Measurement Sets: The first step in reducing the data for all of the samples was to correct for the effect of the Electronic Gate (Egate) on the recorded count rate. In the ims 1280, the beam rasters over the entire area of the measurement in 0.08 s, called the frame time. A measurement cycle consists of adding up the number of 0.08 s frames needed to most closely approximate the requested measurement time for each element in a cycle. Using the Egate means that, for part of each frame, the secondary-ion beam is blanked and does not go into the detector.

When the beam is hitting the electron multiplier, a count rate is recorded, and when the beam is blanked, the recorded count rate is zero. The measured signal in the electron multiplier must be corrected for the dead time of the detector (the time after each event during which the system is not able to record another event; 31 ns in our case). The count rate recorded in the data file is in units of counts per second, which averages the instantaneous count rate, when the beam is in the detector, and zero, when it is not. In order to correct for the dead time of the electron multiplier, we are only interested in the time when the beam is hitting the multiplier; we want to know the instantaneous count rate. To determine the instantaneous count rate, we divide the reported count rate by the fraction of the time when the beam is hitting the detector (in our case 0.36). We can then make a dead time correction.

When the beam is hitting the Faraday cup, the response is different. The characteristic response time of the Faraday cup with a 10^{11} ohm resistor is a few seconds, much slower than the frame time and the rate at which the beam is cycling in and out of the Faraday cup.

The Faraday cup response reaches a steady state that is very close to the value that it would record if the beam was constantly hitting the cup. Thus, we do not make a correction for Egate when using the Faraday cup. The different treatments of the two detectors introduce a small bias between them, but the bias is constant and is only one of several such biases in the measured data. Comparing the measured samples and standards allows us to quantitatively account for these biases.

For the Faraday cups, baseline corrections were made. No correction was made for electron multiplier background, since the correction is only a part in ~10^5 for the background hydrogen and orders of magnitude less for the solar wind and standard implant.

The next step was to perform time interpolation on the data to account for changes in signal strength during the measurement. We first determine the median acquisition time for the $^{1}H^{-}$, $^{16}O^{1}H^{-}$, and $^{12}C^{1}H^{-}$ measurements (the time for the middle of the interval over which data for these species were collected). This is necessary because the count rates are changing rapidly during a depth profile and the count times for the different masses are different. Because the time stamp given in the data file represents the end of the time window, we subtracted half of the measurement time to get the median acquisition time. The time interval between measurements of the same mass is the difference in median acquisition time for a species between measurement cycles. Because the different masses were measured in sequence, the time when a reference mass was measured was different than the times of ^{1}H, $^{16}O^{1}H$, or $^{12}C^{1}H$ measurements. If the count rate of the reference mass is changing, this will result in biased ratios. We therefore performed time interpolation to estimate the count rate of the reference mass at the time when ^{1}H, $^{16}O^{1}H$, or $^{12}C^{1}H$ were measured. The time-interpolated reference count rates were used to calculate $^{1}H/^{16}O$, $^{1}H/^{31}P$, $^{16}O^{1}H/^{16}O_2$, $^{1}H/^{12}C$, $^{12}C^{1}H/^{12}C_2$ ratios used to determine the H fluence.

In order to integrate the standard and solar wind implants, it is necessary to convert the time scale to depth. To do this, we calculated the average sputter rate by dividing the measured crater depth by the time stamp for the last measured mass of the last cycle of the measurement. We multiplied the median acquisition time for ^{1}H by the average sputter rate to get the median acquisition depth. The depth intervals can then be calculated from the median acquisition depths. The beam current was not completely stable during these measurements. For the apatite grains, we could not monitor the beam current during the measurement, but beam current was measured at the beginning and the end of each measurement. The count rates of the reference isotopes, ^{16}O and ^{31}P, serve as secondary monitors of beam current; these isotopes typically show a slow monotonic decrease in count rate. Assuming a linear change in beam current with time, we can estimate the beam current for each cycle of the measurement. For the measurements of Genesis array samples and flight-spare DOS implant standard, we were able to monitor beam current for each cycle. Using the estimated or measured beam currents, a factor was calculated for each cycle by dividing the estimated or measured beam current by the average beam current. This factor was used to adjust the depth intervals for difference in the sputter rate. When the beam current was higher, the sputter rate was higher, so the depth interval was larger, and similarly for lower beam currents. The sum of the adjusted depth intervals was constrained to equal the measured crater depth. Because the change in beam current was small, only a few

percent, we did not attempt to account for the second-order change in relative ionization efficiency that accompanies a change in beam current.

Because we centered the mass peaks every 50 cycles during the measurements, there are several places where the depth interval is just over twice as long as a normal interval. But there is only one measurement for that longer interval. If left alone, this creates a small artifact that affects the final data. To minimize this artifact, we divided these longer intervals into two to simulate what the data would look like had we not done a mass calibration. The count rate originally assigned to the long interval was assigned to the second of these two new intervals (the time stamp is recorded when the counting window closes), and the average of this count rate and the count rate for the previous normal cycle was assigned to the first interval. This gives depth intervals that are similar in length to all the other intervals, and count rates vary smoothly across the cycles.

We are now ready to calculate isotope ratios and integrate the measurements. The details of this integration are discussed for each type of measurement below.

Apatite Standard Measurements: The reason that we included apatite in our implant irradiation was to calibrate the implant against the known water content of the apatite. For the apatite standards, we measured $^{1}H^{-}$, $^{16}O^{-}$, $^{31}P^{-}$, $^{16}O^{1}H^{-}$, and $^{16}O_{2}^{-}$. Apatite is an insulator and so must be measured using the Egun. The Egun provides a few tens of microamps of electrons at close to zero energy to the sample surface to compensate for the positive charge deposited by the Cs^{+} beam. As the electrons pass through the volume above the sample and are decelerated from 10 keV, they pass through an energy regime that effectively ionizes the hydrogen in the gas above the sample. The Egun gives a signal of 100–200 counts per second of H^{-} and 5–7 cps of OH^{-} with the primary ion beam off. We measure this signal by turning off the ion beam at the end of the measurements and collecting data for an addition 30–50 cycles. This background signal is subtracted from the measured H^{-} and OH^{-} signals before any other processing is done.

Count rate profiles for $^{1}H^{-}$, $^{16}O^{-}$, $^{31}P^{-}$, $^{16}O^{1}H^{-}$, and $^{16}O_{2}^{-}$ counts from a measurement of the Lake Baikal apatite, after subtracting the background, correcting for Egate, dead time, and Faraday cup baseline, doing time interpolation, and converting time scales of the profiles to depth scales, are shown in Figs. 6 and 7. Note that the profiles for $^{16}O^{-}$, $^{31}P^{-}$, and $^{16}O_{2}^{-}$ decrease slightly over the course of the measurement. This reflects a slow change in beam current during the measurement and changes in ionization efficiency with crater depth. Although the implant profiles make it hard to evaluate, it looks like the $^{1}H^{-}$ and $^{16}O^{1}H^{-}$ profiles behave the same way. From profiles like these, we calculated $^{1}H/^{16}O$, $^{1}H/^{31}P$, and $^{16}O^{1}H/^{16}O_{2}$ (Fig. 8), giving us three independent measurements of the hydrogen fluence of the standard implant. Before integrating the profiles, we had to account for the artifacts produced by surface hydrogen and for data missing due to presputtering that we did to reduce the contribution from surface hydrogen (from the surface to ~450 Å). To do this, we used the measured shape of the implant profile to extrapolate the profile to zero depth (Fig. 8). Because very little of the implanted ^{1}H resides in this part of the profile, our model of the shallowest part of the profile does not introduce a significant uncertainty into the fluence calculation.

The apatite profiles consist of (1) the intrinsic ^{1}H that was present in the apatite before implantation and (2) the implanted ^{1}H. The ratio profile reaches a baseline value below the standard implant (Fig. 9). This baseline value represents the intrinsic ^{1}H, and the lighter shaded rectangle extending from the bottom of the panel to the baseline in Fig. 9 represents the integrated intrinsic $^{1}H/^{16}O$ profile. The darker shaded area under the ratio curve represents the integrated standard ^{1}H implant. To integrate the profiles, we multiply the ratio value for each cycle by the sputter-rate-adjusted depth interval. Then, we sum the results. (1) The measured profile was integrated, and (2) the intrinsic ^{1}H represented by the lighter rectangle in Fig. 9 was integrated. The difference between the total integral and the intrinsic $^{1}H/^{16}O$ integral is the integral for the implanted $^{1}H/^{16}O$.

$$\text{Total } {}^{1}\text{H}/{}^{16}\text{O} - \text{Intrinsic } {}^{1}\text{H}/{}^{16}\text{O} = \text{Implanted } {}^{1}\text{H}/{}^{16}\text{O} \quad (1)$$

The ratio of the integrated implanted $^{1}H/^{16}O$ to the integrated intrinsic $^{1}H/^{16}O$ can then be multiplied by the ^{1}H content of the apatite to give the fluence of the standard ^{1}H implant:

$$\frac{\text{Implanted H/O}}{\text{Intrinsic H/O}} \times \text{H content of apatite} = \text{H fluence} \quad (2)$$

Data for $^{1}H/^{31}P$ and $^{16}O^{1}H/^{16}O_2$ were processed similar to give independent measurements of the ^{1}H fluence.

Note that as long as the integration meets two criteria, the integration limits do not matter. First, the integration limits must include the entire implanted profile. Second, the integration limits must be the same for both the total profile and the intrinsic $^{1}H/^{16}O$ profile. As an example, the values for the fluence determined from the Lake Baikal Apatite measurement #2 by integrating $^{1}H/^{16}O$ from 0 to 4947 Å (just the implant peak) and from 0 to 7140 Å (the entire depth profile) are 5.99×10^{15} and 6.01×10^{15}, respectively. For $^{1}H/^{31}P$, they are 6.04×10^{15} and 6.07×10^{15}, and for $^{16}O^{1}H/^{16}O_2$, they are 5.66×10^{15} and 5.69×10^{15}, respectively. The data that will be reported in Table 2 were integrated only over the implant peak.

Genesis B/C- and H-Array Collectors: For the B/C- and H-array DOS flight samples, we measure $^{1}H^{-}$, $^{12}C^{-}$, $^{12}C^{1}H^{-}$, and $^{12}C_2^{-}$, and after correcting for the effects of Egate, dead time, and Faraday cup background, the $^{1}H/^{12}C$ and $^{12}C^{1}H/^{12}C_2$ ratios were calculated for each measurement. Although nominally anhydrous, DOS has a measurable intrinsic hydrogen content, and hydrogen is present on and creeps along the sample surface. For these samples, this hydrogen is background and must be accounted for in the data reduction. The depth profiles went through the solar wind profile, then the hydrogen standard implant (implanted at an energy to put it below the solar wind), and then continued deep into the DOS material in order to accurately measure the background hydrogen (Fig. 10). The solar wind and implant profiles are not completely separated, so we used templates for the solar wind and for the standard implant to deconvolve the two profiles (Fig. 11).

Data reduction was done by matching templates for the solar wind and standard implant to the measurements of the implanted Genesis B/C- and H-array collectors, and then integrating the templates. The solar wind templates were measurements of the B/C- and H-array collectors before they were implanted with the standard. The templates were front-side profiles of the collectors and exhibited both surface contamination and low ion yield during the transient period where ion yields had not stabilized. Thus, the shallow portion of the solar wind template had to be estimated. This was done by merging the shallow portion of a simulated profile calculated by SRIM (stopping and range of ions in matter; Ziegler et al. 2010) with the measured profile (Fig. 11). Each solar wind regime has its own SRIM profile. Only the portion of the SRIM profile up to the peak was used. We could not use the entire SRIM profile as a template because hydrogen re-implanted during the measurement distorts the measured profile, especially the zone after the peak of the implant (see the Understanding the Discrepancies between Internal and External Standardization section). Because both the solar wind and standard implant exhibit the same distortion, we did not attempt any corrections for re-implantation.

The standard implant template was obtained from measurements of the flight-spare DOS material. Again, the shallowest part of the template was affected by surface hydrogen and the transient sputtering region. However, the shape of the standard implant profile was amenable to extrapolating the measured template profile to the surface.

Template matching was done by scaling each template both in depth and in ion ratio. The purpose was to match shape of the solar wind and standard implants so that they could be deconvolved in the region where they overlapped. The depth scale of each template was multiplied by a constant to stretch or compress the template to match the measurement. This accounts for slight differences in the measurement conditions between the templates and the samples. Small fixed offsets of 0–10 Å were required to match the solar wind templates to the measurements. No offset was applied to the standard implant templates because no pre-sputtering was used when the standard implants were measured, and there was no evidence that a small offset improved the fits. For the ratio scale, the template baseline was matched to the measurement baseline by adding or subtracting a constant, and the height of the peak was matched by multiplying the measured ratios by a constant. Figure 11 shows an example of the matched templates for one of our B/C measurements. Each template and the matching baseline were then integrated over the same depth range and the integrated baseline was subtracted from integrated template to give the integrated values for the solar wind and the implant standard.

$$\begin{aligned}&\text{Solar Wind Template } {}^{1}\text{H}/{}^{12}\text{C} - \text{Baseline } {}^{1}\text{H}{}^{12}\text{C}\\&\quad = \text{Solar Wind } {}^{1}\text{H}/{}^{12}\text{C}\end{aligned} \tag{3}$$

$$\begin{aligned}&\text{Standard Implant Template} {}^{1}\text{H}/{}^{12}\text{C} - \text{Baseline} {}^{1}\text{H}{}^{12}\text{C}\\&\quad = \text{Implant} {}^{1}\text{H}/{}^{12}\text{C}\end{aligned} \tag{4}$$

The integrated solar wind ratio was then divided by the integrated implant ratio and the result was multiplied by the calibrated fluence of the implant to give the solar wind fluences for the B/C and H arrays.

$$\frac{\text{Solar Wind } {}^{1}\text{H} / {}^{12}\text{C}}{\text{Implant } {}^{1}\text{H} / {}^{12}\text{C}} \times \text{Implant fluence} = \text{Solar Wind H Fluence} \quad (5)$$

The $^{12}C^{1}H/^{12}C_2$ data were treated in the same way. Multiple templates were used to reduce multiple measurements of the solar wind. The means of the resulting fluence estimates were then calculated. The uncertainties on the fluences consist of (1) the 2-sigma standard deviation (SD) of the fluence estimates combined with (2) the uncertainty in the calibration of the hydrogen standard implant. Counting-statistical uncertainties of the measurements were insignificant.

The hydrogen fluences determined for the B/C and H arrays from the $^{1}H/^{12}C$ and $^{12}C^{1}H/^{12}C_2$ ratios are different (see below), with the fluence determined from the molecular ions being systematically lower. This is due to differences in the time evolution of the atomic ion signals and molecular ion signals during the measurement. Charge partitioning between ion species also changes as the sputter crater deepens. While this change in partitioning happens in uniform samples, it may be exacerbated in the DOS because the structure changes with depth because of multiple annealing steps (cf., Sullivan et al. 1998; Jurewicz et al. 2017, 2018). We return to this topic in the Discussion.

Genesis L- and E-Array Collectors: The L- and E-array collectors did not receive a standard hydrogen implant, so their profiles were reduced by comparing to the standard implant in another material (external standardization). There are three choices: the standard implant into flight-spare DOS, the implant into the B/C-array chip, and the implant into the H-array chip. After correcting for the effects of Egate, dead time, and Faraday cup background, the $^{1}H/^{12}C$ and $^{12}C^{1}H/^{12}C_2$ ratios were calculated, as they were for the B/C and H arrays. For the L- and E-array collectors, the measurements were corrected for surface hydrogen and transient sputtering effects using the shallow part of the appropriate SRIM profile, as we did for the B/C- and H-array templates (Fig. 11). The standard profiles used were the templates fitted to the B/C- and H-array implants and the measured profiles in the flight-spare DOS. The profiles in the flight-spare DOS were corrected for surface hydrogen and presputtering by extrapolating the measured profiles to the surface.

The measured E- and L-array profiles and the standard implant were integrated and a constant intrinsic background was integrated over the same depth interval. The background was then subtracted from the total measurements for both solar wind and implant to give the integrated values for each profile (cf. Equations 3 and 4). The integrated solar wind profile was then divided by the integrated standard profile and the result was multiplied by the fluence in the standard implant (Equation 5). The $^{12}C^{1}H/^{12}C_2$ data were treated in the same way.

We also reduced the B/C solar wind profile against the standard implant into the H array and into the flight-spare DOS, and reduced the H solar wind profile against the standard implant into the B/C array and into the flight-spare DOS, to compare and validate the internal and external standardization methods.

Data Reduction Using Counts Per Second Per nanoAmp—The overall philosophy of the data reduction for the DOS collectors using cps/nA was the same as that for ratios described above. We just substituted cps/nA for the ratios. Depth scales were corrected to beam current in the same way and templates were fit to the data and integrated in the same way. In some ways, this method appears to be more robust because the results depend only on the H or CH and not on the substrate. But without a normalizing isotope, we have no direct way to account for changes in ionization efficiency for the ion of interest during a measurement. The cps/nA results are compared to the results calculated from ratios below.

RESULTS

Apatite Standard Measurements

The results of our fluence measurements for our implanted apatite standards are shown in Table 2. Estimates from all three ratios are shown. The fluence estimates from the atomic ratios differ by at most ~1.6% for Crystal Lode and ~3.1% for the Russian apatite. Note that the means of the fluence estimates obtained from the atomic ratios differ by ~6% between the Crystal Lode and Lake Baikal apatites. This difference can be attributed primarily to the values that we are using for their intrinsic water contents (Crystal Lode, 0.37 ± 0.03 wt% H_2O; Lake Baikal, 0.20 ± 0.04 wt% H_2O; McCubbin et al. [2012] supporting information). As discussed above, we use the mean of the inferred implant values determined from the two standards to calibrate our implant standard. Our measured mean implant fluence is lower than the nominal implant value (6×10^{15} H cm^{-2}) by ~4.5%.

The individual implant fluences determined from the atomic ratios for each standard agree well with one another. The molecular ratios give somewhat lower inferred fluences and the fluences show more scatter (Table 2). This larger scatter primarily reflects variations in ionization efficiency of molecular ions over the course of the measurements (see below). Although we do not have a detailed model for how the ionization efficiency evolves in apatite, our experience from DOS indicates that molecular ions are more sensitive in this regard. We therefore use the standard fluences determined from the atomic ratios to calibrate our measurements. Uncertainties are difficult to quantify. The counting-statistical uncertainty is very small because we had 10–15 million hydrogen counts in each measurement. There are uncertainties in modeling the leading edge of the profile and in estimating the level of intrinsic hydrogen in the apatite from the data, which is necessary to determine the relative contributions of intrinsic and implanted hydrogen, among others. Rather than attempting to individually determine these uncertainties, which should be more or less random, we use the scatter of the data as an estimate of our reproducibility (given in Table 2). To these values, the reader should add a ±5% systematic uncertainty from our knowledge of the true water content of our standard apatites.

Internal Standardization for B/C- and H-Array Measurements

Our B/C- and H-array measurements were designed to be internally standardized using a calibrated hydrogen implant into the actual flight samples. The data reduction is described in Data Reduction section. Our results for the B/C and H arrays, calculated using the $^{1}H/^{12}C$ and $^{12}C^{1}H/^{12}C_{2}$ ratios, are summarized in the top line of Table 3. Data for each individual measurement are given in Table S1 in supporting information. For each array, data from two solar wind measurements were reduced using two standard measurements. One solar wind template was used for the B/C array, while two solar wind templates were used for the H array. Two standard templates were used for both B/C and H arrays. The 2σ SDs of the results from $^{1}H/^{12}C$ were ~±1.7% for the B/C array and ~±2.2% for the H array. The fluences determined from $^{12}C^{1}H/^{12}C_{2}$ also agree very well for each set of data, but these results are systematically lower than those determined from $^{1}H/^{12}C$ by ~12% and ~5% for the B/C and H arrays, respectively. This difference reflects a difference in evolution of count rates for atomic ions and molecular ions over the course of a measurement (see below). Fluences reported in Table 3 have been corrected for backscattered hydrogen ions based on SRIM simulations (4% for B/C, 2.64% for H).

External Standardization for B/C-, H-, E-, and L-Array Measurements

External standardization uses a standard implant into different piece of material from that carrying the solar wind, but which has nominally the same composition. External standardization was done using the same standard implant into three different materials (1) flight-spare DOS, (2) the B/C-array chip, and (3) the H-array chip. The B/C array data were standardized against the flight-spare DOS and the H-array standard implant, while the H array data were standardized against the flight-spare DOS and the B/C-array standard implant.

The E and L arrays were each reduced using all three standard materials. At least two solar wind measurements and multiple standard measurements were used to reduce the data.

The externally standardized data obtained using ratios for the B/C and H array are shown in lines 2–4 of Table 3. Data for each individual measurement are given in Table S2 in supporting information. The fluence values calculated using the flight-spare DOS as the external standard (line 2 of Table 3) are all higher than those from the internal standards. This primarily reflects the difference in the way the standard implants were used. For internal standardization, the implants into the flight-spare DOS were treated as templates, the purpose of which was to allow us to deconvolve the deep tail of the solar wind from the shallow tail of the standard implant. The standard template was stretched vertically and horizontally to match the measurement of the internal implant, and then, the template was integrated. This manipulation of the standard template resulted in a 13–20% higher integrated internal standard peak than did integrating the measured standard profile without manipulation. The result is 13–20% lower fluences for the internal standardizations.

When using the B/C internal standard as external standard to reduce the H-array solar wind (and vice versa), the integration of the implant standard peak from the internal standardization was used without modification. The resulting fluence from $^{1}H/^{12}C$ for B/C is

slightly lower than that from the internal standardization, and the fluence for the H array standardized to the B/C internal standard is slightly higher than the internal standardization. For the molecular ratios, standardizing to the internal standard from the other array gives essentially the same answer as the internal standardization (Table 3).

The bottom half of Table 3 shows fluences calculated from cps/nA for the B/C and H arrays. Data for individual measurements are given in Tables S1 and S2. For ^{1}H, the internal standardization using cps/nA gives fluences that are very similar to those calculated from ratios. For the flight-spare DOS external standard, cps/nA gives higher fluences than does the internal standard, but the difference between internal and external standardization for cps/nA is smaller than for the ratios (Table 3). Standardizing the H array with the BC internal standard gives a fluence similar to that from the flight-spare DOS and higher than that from the ratios. The external standardization of the B/C array with the H-array internal standard results in a significantly lower fluence than those obtained from flight-spare DOS or from the ratios (Table 3). For the molecular ions, cps/nA gave higher fluences for the H array than did the ratios, and for the B/C array, the internal standard gave a higher fluence than the ratios, while the external standards gave lower fluences than the ratios (Table 3).

Table 4 shows fluences for the L and E arrays calculated from $^{1}H/^{12}C$ and $^{12}C^{1}H/^{12}C_{2}$ and from ^{1}H and $^{12}C^{1}H$. Data for individual measurements can be found in Table S2. For a given standardization, the fluences calculated from $^{1}H/^{12}C$ vary by 1.8–5.6% for the L array and by 3.0–6.1% for the E array (Table 4; Table S2). There is more variation between the three external standardizations, with estimated fluences for the L and E arrays each varying by ~16%. Similarly, for a given standardization, the fluences calculated from $^{12}C^{1}H/^{12}C_{2}$ vary by 6.5–9.5% for the L array and 6.4–9.7% for the E array, while the variation between standards is ~12%. For both ratios and both arrays, the highest fluence estimates come from the standardization based on the separate flight-spare DOS.

For cps/nA, fluences estimated among measurements for ^{1}H vary by 2.8–6.3% for the L array and 3.1–6.4% for the E array for a single standardization (bottom half of Table 4). Among the three standardizations, fluence estimates based on ^{1}H vary by ~19% for the L array and ~19% for the E array. Similarly for $^{12}C^{1}H$, fluence estimates from cps/nA using a single standard vary by 2.0–4.2% for the L array and by 2.8–3.0% for the E array (Table S2). Among the three standardizations, fluence estimates based on $^{12}C^{1}H$ vary by ~21% for both the L and E arrays (Table 4). The fluences determined for ^{1}H from the flight-spare DOS standardization are higher than those for the other external standards, as was the case for the ratios. However, the fluences determined from the B/C implant standard were highest for $^{12}C^{1}H$ for both the L and E arrays. Fluences determined from $^{12}C^{1}H$ for the L array are greater than or equal to those determined from ^{1}H, but for the E array, all fluences determined from $^{12}C^{1}H$ are lower than those determined from ^{1}H. In many cases, the inferred fluences from cps/nA are quite similar to those determined from the ratios. But because fluences estimated from cps/nA are subject to variations in primary beam current and other artifacts, we use them primarily to help us understand our ratio data (see below).

DISCUSSION

Understanding the Differences in Fluences for $^{1}H/^{12}C$, $^{12}C^{1}H/^{12}C_2$, and cps/nA

As Tables 3 and 4 and Tables S1 and S2 show, there are significant and sometimes systematic differences between fluences calculated from $^{1}H/^{12}C$, $^{12}C^{1}H/^{12}C_2$, and cps/nA. These differences are due primarily to changes in ionization efficiency of the various measured species over the course of a measurement. Consider first what happens to the ^{1}H and $^{12}C^{1}H$ count rates. Figure 12a shows the measured counts for these two species during an analysis of the Genesis E array. Note that the $^{12}C^{1}H$ solar wind peak is lower than the ^{1}H peak, but the baseline for $^{12}C^{1}H$ is higher than that for ^{1}H. Figure 12b shows the measured counts of ^{12}C and $^{12}C_2$. The count rates for both species decrease with time during a measurement, with $^{12}C_2$ decreasing more rapidly than ^{12}C. This decrease reflects changes in ionization efficiency and ion extraction into the mass spectrometer, which have a greater effect on molecular ions than on atomic ions. It is difficult to see the effects of changing ionization efficiency for ^{1}H and $^{12}C^{1}H$ (Fig. 12a) because the solar wind profile dominates. But the end of the measurement likely reaches the background level and so gives an indication of the evolution of ionization sensitivity. Linear regressions through the deepest parts of the two profiles suggest that the ionization efficiency for ^{1}H decreases slightly faster than that for $^{12}C^{1}H$, at least in the deepest part of the profile. The ^{12}C and $^{12}C_2$ count rates also decrease with time (Fig. 12b), with the $^{12}C_2$ count rate decreasing significantly faster than the ^{12}C count rate. The rate of decrease decreases with time as well (the curves are concave upward). Regression of the same cycles as for ^{1}H and $^{12}C^{1}H$ implies that the decreases in count rate for ^{12}C and $^{12}C_2$ are faster than those for ^{1}H and $^{12}C^{1}H$.

Figure 13 shows the $^{1}H/^{12}C$ and $^{12}C^{1}H/^{12}C^{2}$ ratios for the E-array measurement. As expected from Fig. 12, the atomic ratio has a much higher solar wind peak than the molecular ratio. Regressions through the deepest part of the profiles are flat, showing little differential evolution of ionization efficiency. If the ratios did not evolve with time or differ between samples, differences between atomic and molecular ions would not produce different answers because the sample and standard would show the same differences. But for our samples, the ratios do evolve over the measurement (cf. Fig. 12), with the result that standards and samples measured at different depths can have systematic differences in ionization efficiency. A solar wind profile measured with lower relative ionization efficiency of the numerator ion will give a lower inferred fluence if standardized against an implant standard measured with higher relative ionization efficiency of the numerator ion. This is what is happening with the $^{12}C^{1}H/^{12}C_2$ ratio. At the start of the measurement, the $^{12}C^{1}H$ counts are almost as high as the ^{1}H counts (Fig. 12a). The $^{12}C^{1}H$ signal drops more slowly than the ^{1}H signal and at the end of the profile is higher than the ^{1}H signal (Fig. 12a). The $^{12}C_2$ count rate is proportionally significantly higher than the ^{12}C count rate at the beginning of the measurement, and the $^{12}C_2$ count rate drops much more quickly over the measurement (Fig. 12b). As a result, the $^{12}C^{1}H/^{12}C_2$ ratio does not decrease as fast as the $^{1}H/^{12}C$ ratio. A standard implant at ~3000 Å will give a proportionally higher $^{12}C^{1}H/^{12}C_2$ ratio than will the $^{1}H/^{12}C$ ratio compared to the solar wind, so the solar wind fluence estimated from $^{1}H/^{12}C$ will be higher (sample/standard ratio will be higher) than the fluence estimated from $^{12}C^{1}H/^{12}C_2$. This is what our data show (Tables 3 and 4).

Which ratio is more reliable? Our test of how ionization efficiency changes as the measurement spot approaches a boundary (see the Experimental Difficulties and Their Solutions section) shows that the molecular-ion ratios are much more sensitive to the boundary effect than atomic-ion ratios. Tables 3 and 4 show more variability in the fluences determined from the molecular ratios than for the atomic ratios, other things being equal. These observations suggest that the atomic ions are more reliable.

Is the atomic ratio giving an accurate fluence measurement? The evolution of both ^{12}C and $^{12}C_2$ appears to be faster than the evolution of ^{1}H and $^{12}C^{1}H$ during a measurement (Figs. 12 and 13). The direction of the evolution suggests that both the atomic and molecular ratios are giving fluences that are lower than the true values, although the $^{1}H/^{12}C$ ratio shows less of this effect. There is one other subtle effect on the atomic ions. A high dose of ^{1}H implanted into DOS causes the ion yield for ^{12}C to go down. This can be observed in the B/C array samples, which show dips in the ^{12}C count rate under the solar wind peak and under the standard peak (Fig. 14). The same effect is not observed for $^{12}C_2$. If this effect is proportional to the ^{1}H concentration, then it should not affect the final fluences because the ratio of ^{1}H concentration to ^{12}C depression in solar wind and standard implant should be the same.

Cps/nA potentially provides an independent way of evaluating the data. When using ratios, the results are affected by variations in both numerator and denominator. This can be good if the two species vary in the same way, such as when the ion probe primary beam current changes. However, if the species vary independently, such as if the ionization efficiencies of the numerator and denominator vary at different rates as the ion probe pit gets deeper, these changes can be a problem. In our data set, cps/nA for ^{1}H give results similar to the $^{1}H/^{12}C$ ratios for the internally standardized B/C and H arrays (Table 3). $^{12}C^{1}H$ gives higher internally standardized fluences than $^{12}C^{1}H/C_2$. For the B/C array, the $^{12}C^{1}H$ fluence from cps/nA is still lower than that from the $^{1}H/^{12}C$ ratio, but for the H array, the cps/nA give essentially the same fluence from both $^{12}C^{1}H$ and the $^{1}H/^{12}C$ ratio (Table 3). The close agreement between the fluences obtained from $^{1}H/^{12}C$ and from cps/nA for ^{1}H for the internal standardization supports our preference for using the atomic ratios to infer the hydrogen fluences for the B/C and H arrays. The scatter of the molecular-ion data reinforces our decision not to use the molecular ions. The different external standardizations for cps/nA for the B/C and H arrays give variable results, with both higher and lower fluences from cps/nA compared to ratios. These data provide no reason to prefer the external standardization. Our preferred fluences for the B/C and H arrays are thus those from the atomic ratios using the internal standardization.

Fluences for the E and L arrays determined for the flight-spare DOS from cps/nA of ^{1}H and $^{12}C^{1}H$ are somewhat lower than those determined from the ratios (Table 4). When the L and E arrays are standardized using the internal B/C standard, the atomic ratios and cps/nA give similar fluences. The internal H-array standard gives lower fluences for the L and E arrays from cps/nA than from the ratios (Table 4). For the atomic ions, cps/nA show more scatter in the fluence estimates than do atomic ratios. This may be because the ratios account for variability due to changes in source strength. We will use fluences from the atomic ratios from this point on. Comparisons among cps/nA and ratios do not provide a strong reason for

choosing one standard over another for the L and E arrays. We investigate this further in the next section.

Understanding the Discrepancies Between Internal and External Standardization

As discussed above, fluences calculated from the $^{1}H/^{12}C$ and $^{12}C^{1}H/^{12}C_2$ ratios for the B/C and H arrays using internal and external standardization can show very large differences (Table 3). The difference between fluences determined by internal standardization and by external standardization using the implant into the flight-spare DOS material are particularly large. As discussed in Internal Standardization for B/C- and H-Array Measurements section, when using the implants in DOS as an external standard, we integrate the implant profile directly to standardize the solar wind profile. We also use the same profiles as templates to help us deconvolve the solar wind from the internal standard implant in the B/C and H arrays. When used as a template, the standard profiles from the flight-spare DOS material were stretched both vertically (~6.5% to 10%) and horizontally (~6% to 10.5%) to fit the standard implant in the B/C and H arrays. This results in the internal standard having a ~12% to 15% higher integral, which translates into a 12–15% lower fluence for the B/C and H collectors. The question now is, why should the same implant into different DOS samples, supposedly analogous materials, give different integrations and thus, different fluences?

One possibility is that the implant was heterogeneous and different DOS pieces got different implant doses. But a variety of tests of various implants from Kroko, Inc. (e.g., Burnett et al. 2015) and the carefully designed raster system of the implanter assure that the implant is homogeneous to better the 1% over an area of ~4 × 4 inches, significantly larger than the target that we implanted. If the implant fluence were spatially heterogeneous, the heights of the implant peaks should have been different, reflecting the variable fluence, and the depth of the implant should have been the same across all DOS materials in the target, assuming the materials were the same. But the templates for our implants into the BC and H arrays are stretched in both height and depth, so implant heterogeneity is not the answer. Another possibility is that the average densities of the DOS pieces are different. But in this case, the depth scale and the vertical scale should anticorrelate to preserve the area under the curve. By themselves, differences in density cannot explain what we observe.

A third possibility is that the relative ionization efficiencies differed among the measurements. In their measurements of Mg^{+} ion sputtered by an O_2^{+} beam, Jurewicz et al. (2017) showed that the relative ion yields of the molecular $^{12}C_2^{+}$ and atomic $^{12}C^{+}$ ions can vary as a function of both composition (the presence of silicon) and local bonding environment (size and distribution of nonconductive sp^3 structures versus conductive sp^2 structures) in diamond-like carbon. The variations in ion yield with structural elements of the matrix were enhanced because O_2^{+} was used for the analyses. Pure carbon chemically etches under an oxygen beam, while silicon-rich matrices sputter in the expected manner.

It is reasonable to assume that during sputtering by a Cs^{+} beam, the relative ion yield for ^{1}H and $^{12}C^{1}H$ could also change as a function of the composition and bonding structure of the matrix. We investigated several properties of the collectors looking for correlations with ionization efficiency. We tried parameterizations using (1) the calculated $^{12}C_2^{-}/^{12}C^{-}$ ratio for each measurement, both before the implant peak and at 30–50 Å after the implant peak,

and (2) the sputtering rate. We also carried out SEM and Raman investigations of the analysis pits in the standards and samples, looking for excess silicon or SiC. We found differences on some of these properties from spot to spot. Unfortunately, our data set is too sparse and did not show internally consistent results. Therefore, based on the limited systematics we found between atomic and molecular ions and ratios and cps/nA (see above), we decided to use the internal standardization of the B/C and H arrays. Because the B/C and H arrays seem to be different than the flight-spare DOS, and because we would expect the different flight samples of DOS to be more similar to one another than to a sample of flight-spare DOS, we used the average of the internal B/C and H standards to reduce the data for the E and L arrays. Our final results, using the $^{1}H/^{12}C$ ratios and standardized as just described, are shown in Table 5.

Comparison with the Genesis Ion Monitor

On board the Genesis spacecraft, solar wind conditions were recorded by the Genesis Ion Monitor (GIM). The purpose of the GIM was to determine which solar wind regime was impacting the collectors during specific times, thus determining which collector should be unshaded (Neugebauer et al. 2003; Reisenfeld et al. 2013). The hydrogen fluences determined by the GIM are compared with our fluence values in Table 5. The fluences determined from this study are lower than those determined by the GIM, ranging from ~87% of GIM values for the H and E arrays to ~68% for the L array. Note that the arrays that collected high-energy solar wind (H and E arrays) have higher fluences compared to the GIM than the other arrays.

Why are our values lower than those from the GIM? One possibility is that our standard calibration is off. If we are using low values for the water content of our apatite standards, our results could be systematically low. Perhaps the DOS collectors are not as retentive for hydrogen as we assumed and diffusive losses have occurred. However, Heber et al. (2009b) found in experiments with DOS and helium that diffusive loss was negligible, implying that diffusive loss is not an issue. There may also be some uncorrected or unrecognized artifacts in our data reduction. As discussed above, it is possible that our numbers are systematically low due to evolution of ion yields with depth in the ion probe craters. But we do not believe that this could introduce more than a ~5% systematic error, not enough to explain the differences.

Using SRIM (Ziegler et al. 2010), we calculated model implant profiles for the solar wind from each solar wind regime into the DOS collectors. These calculations used energy profiles determined from the GIM (Reisenfeld et al. 2013), and assumed densities for the DOS collectors of 2.75, 2.85, and 2.9 g cm^{-3}. We modeled the shallow portion of the solar wind profile, where ion yields in the ion probe have not yet reached equilibrium, with SRIM profiles. However, SRIM may overestimate the depth of the implant for the lowest energies because it does not take into account mechanisms for dissipation of energy when there is a large band gap restricting the free flow of electrons in the material. Diamond has a large band gap and is not modeled accurately by SRIM (Ziegler, personal communication). Although diamond-like carbon is not pure diamond, sp^3 bonding is a significant component, to the extent that it can be shown to cause variations in electrical conductivity within a single

sample (Sullivan et al. 1998). An empirical result for Mg^+ ions (reported in Jurewicz et al. 2017) is that more of the ions are stopped near the collector surface than predicted by SRIM, and our modeling of the shallow part of the profile would miss a fraction of the implanted solar wind ions. This effect could be greater for regimes with lower energy solar wind (L and B/C arrays), as implied by the comparison of our data with the GIM results. We do not currently have a better way of treating the shallow portions of our profiles, so we have not corrected the data for this type of effect.

Comparison of Measured Profiles with SRIM Profiles

During our study, we noted significant differences in the overall depth and shape of the SRIM profiles compared to our measured solar wind profiles. Figure 15 shows the calculated SRIM profile for the E array compared to a measured profile. The SRIM profile has been scaled vertically to match the measured profile at the peak. The depth scale has not been modified. The SRIM profile is not as broad as the measured profile. This is because some of the hydrogen atoms in the Genesis sample that are hit by the primary ion beam are either pushed deeper into the sample (gardening or knock-on effect) or are redeposited into the sample, making them available to be sputtered again, thereby broadening the profile.

The effect of gardening can be estimated from the decay of surface contamination as it is sputtered away by the primary ion beam. Figure 15 also shows how the signal of the gardened surface hydrogen decays away at the beginning of the measurement along with a power-law model for that decay (solid line). Gardened in hydrogen is still contributing to the signal well into the implant. The implant itself can also be gardened in, but it is not easy to recognize. The measured hydrogen signal includes a component of gardened-in hydrogen throughout the measurement (surface hydrogen in the shallow profile, implant hydrogen throughout). The fraction of implant hydrogen that is gardened in is small, considerably smaller than the contribution of the surface hydrogen to the shallow part of the profile. But some distortion of the implant profile does occur.

A more significant distortion of the profile comes from sputtered hydrogen that is re-implanted. Hydrogen atoms sputtered by a Cs^+ primary-ion beam efficiently make H^- ions, but H^+ ions are also produced. The positive ions are accelerated back into the sample because the sample surface is set to −10 keV. The relative efficiency of production of positive and negative ions is hard to measure in an ion probe because only one species can be measured at a time, and retuning the instrument to measure ions of the opposite polarity changes the relative efficiency of production of positive and negative ions. A comparison of the FIP of hydrogen (~13.6 eV) with the electron affinity (~0.75 eV) implies that it is ~18 times less probable to produce an H^+ ion than an H^- ion. Systematic studies of RSFs suggest that the H^-/C^- yield is roughly 10 times higher than the H^+/C^+ (e.g., Wilson 1995). But even a few percent of re-implanted ions will spread the measured depth profile in a manner similar to gardening. Figure 16 shows an H^- image of the crater produced during a depth profile through solar wind on DOS. The dark square in the middle is the measurement region, and the brighter area around the square is hydrogen sputtered from the square and re-implanted around it. Even more hydrogen was re-implanted into the square itself, but it has been re-sputtered and eliminated from the square. Although is it not possible to quantify re-

implanted hydrogen from this image, it is clear that hydrogen is re-implanted during these measurements.

Together, re-implantation and gardening are primarily responsible for the differences between the SRIM profiles calculated for the Genesis collectors using models of the actual energies of the solar wind ion that were implanted. Therefore, we cannot use the SRIM profiles as templates for the ion probe measurements. We did use the shallow part of the SRIM profile to model the solar wind profiles in the transient sputtering regions (see the Data Reduction section), and this may be problematic for other reasons (see the Comparison with the Genesis Ion Monitor section). But because the amount of surface hydrogen is decreasing rapidly with depth over this region, the effects of gardening and re-implantation are less on the shallow side of the implant than at the peak of the implant and deeper.

Elemental Fractionations in the Solar Wind

The acceleration of solar wind from the Sun's surface produces elemental fractionations that make it difficult to use solar wind to determine the bulk composition of the Sun's photosphere. Figure 17 shows the ratios of several elements to oxygen in two solar wind regimes normalized to the same ratios in the solar photosphere, plotted versus the FIP. Elements with FIP less than ~10 eV are enhanced in the low-speed solar wind relative to the solar photosphere by a factor of ~2.5 to 3 (e.g., Bochsler 2007a). Elements with high FIP tend to be close to solar abundances (Fig. 17). Coronal hole wind is less fractionated due to FIP than the low-energy wind (Fig. 17; e.g., Bochsler 2007a; von Steiger and Zurbuchen 2016). FIP fractionation has been characterized in terms of low-FIP and high-FIP plateaus, but Fig. 17 does not show convincing plateaus. Instead, there seems to be a relatively smooth fractionation as a function of FIP. Hydrogen, with a FIP of 13.6 eV, is transitional between low- and high-FIP elements and can potentially help us to understand these fractionation processes.

We now have high-quality Genesis data for hydrogen, helium, neon, and argon in bulk solar wind (B/C array), interstream wind (L array), coronal hole wind (H array), coronal mass ejections (E array). All regimes of the solar wind are composed almost entirely of hydrogen. Calculating abundance ratios of heavier elements relative to hydrogen allows for the clearest physical interpretation of fractionations of heavier elements in the different solar wind regimes. To investigate whether these regimes show differences in fractionation as a function of FIP, we have plotted the hydrogen, argon, neon, and helium data for the four regimes as ratios to hydrogen versus FIP (Fig. 18). The elemental ratios are normalized to the same ratios in the H array, because coronal-hole wind is considered to be the least fractionated of the regimes (Bochsler 2007a; von Steiger and Zurbuchen 2016). Clear regularities are apparent in Fig. 18. The E array shows the greatest enrichments of noble gases relative to the other arrays, with enrichment increasing as a function of FIP. Coronal mass ejections can be significantly enriched in helium (Borrini et al. 1982). The cause of helium enrichments in some CMEs is not currently understood, though a helium-enriched plasma was proposed by Hirshberg et al. (1972) to drive the shock that generates the type II radio burst associated with coronal mass ejections. The correlation between the degree of enrichment of argon, neon, and helium relative to hydrogen and FIP suggests a role for FIP in the fractionation of

these elements in coronal mass ejections. The L array is also enriched in helium, neon, and argon relative to the H array. Although much smaller, the enrichments also increase with increasing FIP. The B/C array, which captures solar wind from all regimes, shows small enrichments consistent with a mixture of gases from the E, L, and H arrays.

The Composition of the Solar Photosphere and the Metallicity of the Sun

Prior to ~2003, published estimates of the abundances in the solar photosphere determined from spectroscopy were consistent with those obtained by helioseismology (e.g., Basu and Antia 2004, 2008). However, in the late 1990s and early 2000s, the models used to convert measured line properties into photospheric abundances underwent a revolution, with relaxation of the assumption that the lines originated in local thermodynamic equilibrium, the application of 3D descriptions of the motions in the Sun's atmosphere, and new values for opacities and other parameters (e.g., Asplund 2005; Grevesse et al. 2007; Asplund et al. 2009). These changes resulted in significantly lower abundance estimates for the carbon, nitrogen, and oxygen in the Sun (26%, 40%, and 42%, respectively, compared to values given by Anders and Grevesse 1989). The low abundances cannot be reconciled with the properties of the Sun as inferred by helioseismology (e.g., Basu and Antia 2008). This discrepancy has not been resolved.

Von Steiger and Zurbuchen (2016) propose that abundances from coronal hole solar wind can be used directly as photospheric abundances (for all elements except He) because FIP fractionation is small for this regime. Based on data from the solar-polar-orbiting *Ulysses* spacecraft, they conclude that the helioseismology metallicity (dominated by CNO abundances) is correct. However, coronal hole FIP models by Laming (e.g., Laming et al. 2017) predict that H/Mg is depleted to 0.46 of the Asplund et al. (2009) photospheric abundances. Furthermore, the reprocessing of *ACE* data by Pilleri et al. (2015) shows that the coronal hole O/Mg ratio is fractionated: 0.63 of the Asplund et al. (2009) photospheric value in the Genesis sampling period. *Ulysses* directly sampled the purest coronal hole material from the solar poles, but von Steiger and Zurbruchen show (their fig. 2) that ecliptic coronal hole material (e.g., the Genesis H array sample) has the same composition as the polar hole material. Hydrogen has essentially the same FIP as oxygen. Thus, the Genesis H array hydrogen fluence should also show minimal fractionation. An accurate Genesis H array–photosphere comparison can be made with He/H. Using helium fluences from Heber et al. (2012), the Genesis H-array He/H (0.0567 ± 0.0007) is significantly higher (less fractionated, as expected) than the Genesis bulk He/H (0.0508 ± 0.0003) or the L array He/H (0.0505 ± 0.0035), but still well below the helioseismology solar He/H (0.084 ± 0.002).

The neon abundance in the photosphere cannot be directly measured spectroscopically because neon has no absorption or emission lines in the photosphere. This led to the suggestion that a higher neon abundance might counterbalance the effect of lower abundances of carbon, nitrogen, and oxygen (e.g., Bahcall et al. 2005), but the level of neon enrichment required to make photospheric abundances and helioseismology consistent can probably be ruled out (e.g., Bochsler 2007b). The neon abundance can be inferred from X-ray and UV spectroscopy of the solar corona, solar flares, and even solar wind. However, interpreting these data is complicated by the FIP effect (see above). A common approach is

to determine the neon abundance relative to a reference element (e.g., oxygen) in the solar corona and assume the ratio is the same in the photosphere (Asplund et al. 2009). Although both oxygen and neon are high-FIP elements, there is a significant difference in FIP between them (oxygen, 13.6 eV; neon 21.6 eV) that could cause fractionation in the solar wind (see the Elemental Fractionations in the Solar Wind section). Estimates of solar neon abundance made prior to Genesis results include (using the logarithmic scale where the hydrogen abundance is defined as log ϵ_H=12.00): log ϵ_{Ne} = 7.87 ± 0.10 (Lodders 2003), 7.93 ± 0.10 (Asplund et al. 2009), log ϵ_{Ne} = 7.96 ± 0.13 (Bochsler 2007b), log ϵ_{Ne} = 8.09 ± 0.10 (Anders and Grevesse 1989).

Solar wind fluences for hydrogen and the noble gases from the Genesis mission provide an independent determination of the neon abundance in the Sun. Here, we use our hydrogen fluences and the helium and neon fluences for the four solar wind regimes (Heber et al. (2009b, 2012; Heber, personal communication). Hydrogen is a moderately high-FIP element with a FIP of 13.6 eV, essentially identical to oxygen. Figure 19a plots $^{20}Ne/^{4}He$ against $^{1}H/^{4}He$ for the four solar wind regimes. Extrapolating a line fit to the data to the solar $^{1}H/^{4}He$ ratio (11.9 ± 0.17; Basu and Antia 2008) gives the $^{20}Ne/^{4}He$ ratio in the Sun, which in turn gives a $^{20}Ne/^{1}H$ ratio of (1.07 ± 0.08) × 10^{-4}. Neon-20 makes up 93% of solar neon (Heber et al. 2012), so our $^{20}Ne/^{1}H$ ratio gives a total Ne/H ratio of (1.15 ± 0.09) × 10^{-4}. From this, we calculate a solar neon abundance of log ϵ_{Ne} 8.060 ± 0.033. Note that using the data from the GIM in the same way gives an essentially identical solar neon abundance of log ϵ_{Ne} 8.057 ± 0.033. Our value for the solar neon abundance is within the range of previous estimates, but is somewhat higher than the more recent estimates. It is not high enough to resolve the disagreement between spectroscopy and helioseismology.

The argon abundance in the Sun can be inferred from spectroscopic measurements of solar flares and energetic particles, by nucleosynthesis theory in which nuclear statistical equilibrium allows a prediction based on nearby α-elements ^{28}Si and ^{40}Ca, by measurements of argon in iron meteorites, and by comparison with Jupiter's atmosphere (e.g., Lodders 2008; Asplund et al. 2009). Asplund et al. (2009) use several techniques to estimate log ϵ_{Ar} = 6.40 ± 0.13, while Lodders (2008) estimate log ϵ_{Ar} = 6.50 ± 0.10. We use the same technique as used above (Fig. 19b) to estimate an $^{36}Ar/^{1}H$ ratio in the solar photosphere of 2.03 × 10^{-6}, which, when corrected for isotopic abundances corresponds to a total argon to hydrogen ratio of 2.41 × 10^{-6} and a log ϵ_{Ar} = 6.38 ± 0.12. Our value is very similar to the estimate from Asplund et al. (2009).

Our approach to estimating the neon and argon abundances in the Sun is model independent, but is totally empirical and assumes that extrapolation to the solar Ne/He and Ar/He is valid. Our quoted errors come from propagating the measurement errors. We have not tried to estimate systematic errors, such as differences in the degree of FIP fractionation (small) or other differences in fractionation among the regimes, but we expect these effects to be small.

CONCLUSIONS

We have measured the hydrogen fluences of four different solar wind regimes collected by NASA's Genesis mission. We had to overcome a wide variety of experimental issues to get

reliable data, but we were, for the most part, successful. Our relative fluence numbers are good to ±5–6%, and the absolute fluences are good to ±10%. Compared to results from the GIM, our values are somewhat lower (~12–13% for the E and H arrays; 21% for the B/C array, and ~32% for the L array).

We used our results to evaluate solar wind abundances of hydrogen, helium, neon, and argon in light of FIP fractionations in the solar wind. We found that, when the noble gas abundances are normalized to hydrogen and to the data for the high-energy coronal-hole H-array, the relative abundances for coronal mass ejections (E-array) increase smoothly with increasing FIP. The L array shows similar, but smaller, fractionations.

Using our data and regime data for helium, neon, and argon, we obtained estimates of the neon and argon abundances in the Sun. Our neon abundance estimate is somewhat higher than the currently favored values, but is not high enough to resolve the discrepancy between spectroscopy and helioseismology in modeling the solar structure. Our argon value is at the low end of recent abundance determinations using other methods.

Supplementary Material

Refer to Web version on PubMed Central for supplementary material.

Acknowledgments

We thank the Genesis curatorial facility at JSC for working with us to get the right samples for this work. The paper benefited from a thoughtful review by Martin Laming. Supported by NASA grants NNX09AC32G, NNX14AF25G, and NNX17AE73G to G.R.H. and NNX09AC35G, NNX14AF26G, and 80NSSC17K0025 to D.S.B.

REFERENCES

Anders E and Grevesse N 1989 Abundance of the elements: Meteoritic and solar. Geochimica et Cosmochimica Acta 53:197–214.

Asplund M 2005 New light on stellar abundance analyses: Departures from LTE and homogeneity. Annual Reviews of Astronomy and Astrophysics 43:481–530.

Asplund M, Grevesse N, Sauval AJ, and Scott P 2009 The chemical composition of the Sun. Annual Reviews of Astronomy and Astrophysics 47:481–522.

Bahcall JN, Basu S, and Serenelli AM 2005 What is the neon abundance of the Sun? Astrophysical Journal 631:1281–1285.

Basu S and Antia HM 2004 Constraining solar abundances using helioseismology. Astrophysical Journal Letters 606: L85–L88.

Basu S and Antia HM 2008 Helioseismology and solar abundances. Physics Reports 457:217–283.

Bochsler P 2000 Abundances and charge states of particles in the solar wind. Reviews of Geophysics 38:247–266.

Bochsler P 2007a Minor ions in the solar wind. The Astronomy and Astrophysics Review 14:1–40.

Bochsler P 2007b Solar abundances of oxygen and neon derived from solar wind observations. Astronomy and Astrophysics 471:315–319.

Bochsler P, Auchere F, and Skoug RM 2006 He-H fractionation in the solar wind. How much is due to inefficient Coulomb drag? Proc. SOHO 17 Conference, Taormina ESA SP 617.

Borrini G, Gosling JT, Bame SJ, and Feldman WC 1982 Helium abundance enhancements in the solar wind. Journal of Geophysical Research: Space Physics 87:7370–7378.

Burnett DS 2013 The Genesis solar wind sample return mission: Past, present, and future. Meteoritics & Planetary Science 48:2351–2370.

Burnett DS, Barraclough BL, Bennett R, Neugebauer M, Oldham LP, Sasaki CN, Sevilla D, Smith N, Stansbery E, Sweetnam D, and Wiens RC 2003 The Genesis discovery mission: Return of solar matter to Earth. Space Science Reviews 105:509–534.

Burnett DS, Jurewicz AJG, Woolum DS, Wang J, Paque JM, Nittler LR, McKeegan KD, Humayan M, Hervig R, Heber VS, and Guan Y 2015 Ion implants as matrix-appropriate calibrators for geochemical ion probe analyses. Geostandards and Geoanalytical Research 39:265–276.

Burnett DS, Jurewicz AJG, and Woolum DS 2019 The future of Genesis science. Meteoritics & Planetary Science 54:1092–1114. [PubMed: 31130804]

Grevesse N, Asplund M, and Sauval AJ 2007 The solar chemical composition. Space Science Reviews 130:105–114.

Heber VS, Wiens RC, Bochsler P, Wieler R, and Burnett DS 2009a Fractionation processes in the solar wind revealed by noble gases collected by Genesis regime targets (abstract #2503). 40th Lunar and Planetary Science Conference CD-ROM.

Heber VS, Wieler R, Baur H, Olinger C, Friedmann TA, and Burnett DS 2009b Noble gas composition of the solar wind as collected by the Genesis Mission. Geochimica et Cosmochimica Acta 73:7414–7432.

Heber VS, Wiens RC, Jurewicz AJG, Bogel N, Reisenfeld DB, Baur H, McKeegan KD, Wieler R, and Burnett DS 2011 Isotopic and elemental fractionation of solar wind implanted in the Genesis concentrator target characterized and quantified by noble gases. Meteoritics & Planetary Science 46:493–512.

Heber VS, Baur H, Boschsler P McKeegan KD, Reisenfeld DB, Wieler R, and Wiens RC 2012 Isotopic fractionation of solar wind: Evidence from fast and slow solar wind collected by the Genesis mission. Astrophysical Journal 759:121–135.

Heber VS, McKeegan KD, Bochsler P, Duprat J, and Burnett DS 2014 The elemental composition of solar wind with implications for fractionation processes during solar wind formation (abstract #2117). 45th Lunar and Planetary Science Conference CD-ROM.

Hirshberg J, Bame SJ, and Robbins DE 1972 Solar flares and solar wind helium enrichments: July 1965-July 1967. Solar Physics 23:467–486.

Huss GR, Nagashima K, Jurewicz AJG, Burnett DS, and Olinger CT 2012 The isotopic composition and fluence of solar-wind nitrogen in a Genesis B/C-array collector. Meteoritics & Planetary Science 47:1436–1448.

Jurewicz AJG, Burnett DS, Woolum DS, McKeegan KD, Heber V, Guan Y, Humayun M, and Hervig R 2011 Solar-wind Fe/Mg and a comparison with CI chondrites (abstract #1917). 42nd Lunar and Planetary Science Conference CD-ROM.

Jurewicz AJG, Burnett DS, Rieck KD, Hervig R, Friedmann TA, Williams P, Daghlian CP, and Wiens R 2017 Understanding heterogeneity in Genesis diamond-like carbon films using SIMS analysis of implants. Journal of Materials Science 52:11,282–11,305.

Jurewicz AJG, Koeman-Shields E, Huss G, and Daghlian C 2018 Raman as a tool for quantifying SIMS analyses of Genesis DOS collectors (abstract #2058). 49th Lunar and Planetary Science Conference, E-poster.

Jurewicz AJG, Reick KD, Hervig R, Burnett DS, Wadhwa M, Oligner CT, Wiens R, Laming JM, Guan Y, Huss GR, Reisenfeld DB, and Williams P 2020 The Mg isotopic composition of the bulk solar wind from Genesis DoS collectors. Meteoritics & Planetary Science. 10.1111/maps.13439.

Laming JM, Heber VS, Burnett DS, Guan Y, Hervig R, Huss GR, Jurewicz AJG, Koeman-Shields EC, McKeegan KD, Nittler LR, Beisenfeld DB, Rieck KD, Wang J, Wiens RC, and Woolum DS 2017 Determining the elemental and isotopic composition of the pre-solar nebula from Genesis data analysis: The case of oxygen. Astrophysical Journal Letters 851:L12 (6 pp).

Lodders K 2003 Solar system abundances and condensation temperatures of the elements. Astrophysical Journal 591:1220–1247.

Lodders K 2008 The solar argon abundance. Astrophysical Journal 674:607–611.

Marty B, Chaussidon M, Wiens RC, Jurewicz AJG, and Burnett DS 2011 A ^{15}N-poor isotopic composition for the solar system as shown by Genesis solar wind samples. Science 332:1533–1536. [PubMed: 21700869]

McCubbin FM, Hauri EH, Elardo SM, Vander Kaaden KE, Wang J, and Shearer CK 2012 Hydrous melting of the Martian mantle produced both depleted and enriched shergottites. Geology 40:683–686.

McKeegan DK, Kallio APA, Heber VS, Jarzebinski G, Mao PH, Coath CD, Kunihiro T, Wiens RC, Nordholt J, Moses RW Jr, Reisenfeld DB, Jurewicz AJG, and Burnett DS 2011 The oxygen isotopic composition of the Sun inferred from captured solar wind. Science 332:1528–1532. [PubMed: 21700868]

Meshik A, Hohenberg C, Pravdivtseva O, and Burnett D 2014 Heavy noble gases in solar wind delivered by Genesis mission. Geochimica et Cosmochimica Acta 127:326–347. [PubMed: 29151613]

Neugebauer M, Steinberg JT, Tokar RL, Barraclough BL , Dors EE, Wiens RC, Gingerich DE, Luckey D, and Whiteaker DB 2003 Genesis on-board determination of the solar flare regime. Space Science Reviews 105:661–679.

Pilleri P, Reisenfeld DB, Zurbuchen TH, Lepri ST, Shearer P, Gilbert JA, von Steiger R, and Wiens RC 2015 Variations in solar wind fractionation as seen by *ACE/SWICS* and the implications for *Genesis* mission results. The Astrophysical Journal 812:1–10.

Reames DV 2018 The “FIP effect” and the origins of solar energetic particles and of the solar wind. Solar Physics 293:47.

Reisenfeld DB, Wiens RC, Barraclough BL, Steinberg JT, Neugebauer M, Raines J, and Zurbuchen TH 2013 Solar wind conditions and composition during the Genesis mission as measured by in situ spacecraft. Space Science Reviews 175:125–164.

Rieck KD 2015 Solar wind sodium and potassium abundance analysis in Genesis diamond-on-silicon and silicon bulk solar wind collectors, and how hydration affects the microtexture of olivine phase transformation at 18 GPa. PhD dissertation, Arizona State University, online.

Rieck KD, Jurewicz AJG, Burnett DS, Hervig RL, Williams P, and Guan Y 2016 Bulk solar wind Na and K measured in Genesis collectors (abstract #2922). 47th Lunar and Planetary Science Conference CD-ROM.

von Steiger R and Zurbuchen TH 2016 Solar metallicity derived from in situ solar wind composition. Astrophysical Journal 816:13 (8 pp).

Sullivan JP, Friedmann TA, Dunn RG, Stechel EB, Schultz PA, Siegal MP, and Missert N 1998 The electronic transport mechanism in amorphous tetrahedrally-coordinated carbon films. Materials Research Society Symposium. Proceedings 498:97–102.

Westphal AJ, Ogliore RC, Huss GR, Nagashima K, and Olinger CT 2014 Mg profile correction in Genesis Si collectors using rastered ion imaging (abstract #2671). 45th Lunar and Planetary Science Conference CD-ROM.

Wilson RG 1995 SIMS quantification in Si, GaAs, and diamond—An update. International Journal of Mass Spectrometry and Ion Processes 143:43–49.

Ziegler JF, Ziegler MD, and Biersack JP 2010 SRIM—The stopping and range of ions in matter (2010). Nuclear Instruments and Methods in Physics Research B 268:1818–1823.

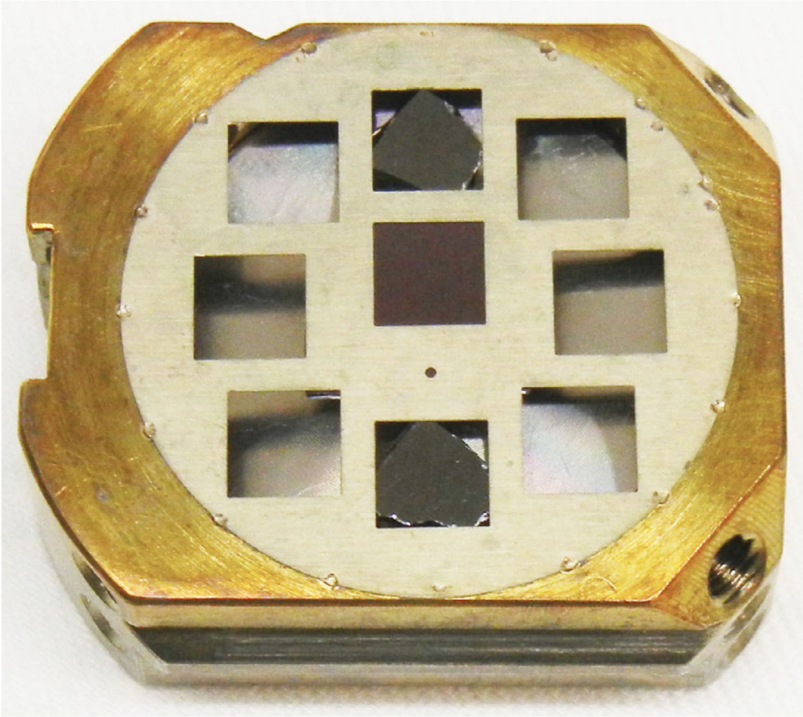

Fig. 1.

Cameca sample holder with Genesis collectors and DOS standard mounted behind mask with 6 mm holes. H array top, DOS standard middle, B/C array bottom.

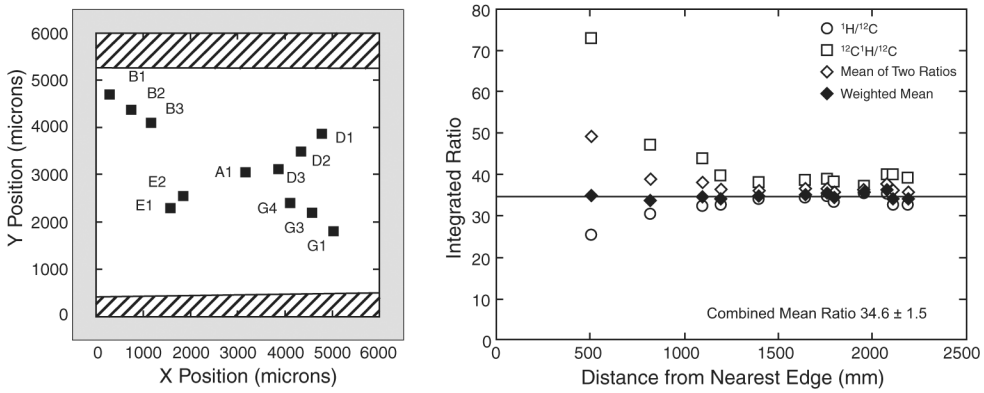

Fig. 2.

Map of measurement spots on a standard H implant into DOS (left) and the $^{1}H/^{12}C$ and $^{12}C^{1}H/^{12}C_{2}$ ratios obtained from those spots (right). The sample (white) was mounted behind a mask (gray). The hatched areas are void spaces. The $^{1}H/^{12}C$ and $^{12}C^{1}H/^{12}C_{2}$ ratios vary significantly with distance from the nearest edge. The measured ratios diverge as the extraction field of the mass spectrometer is distorted by an edge. We also plot the average of the two ratios and a weighted mean with the weighting factors chosen to give a consistent mean independent of the absolute values of the measured ratio (the elemental ratio was given a weight of 0.85 and the molecular ratio was given a weight of 0.15). The average of the weighted means (labeled Combined Mean Ratio and shown by the horizontal line) and the 2σ SD of the data are given.

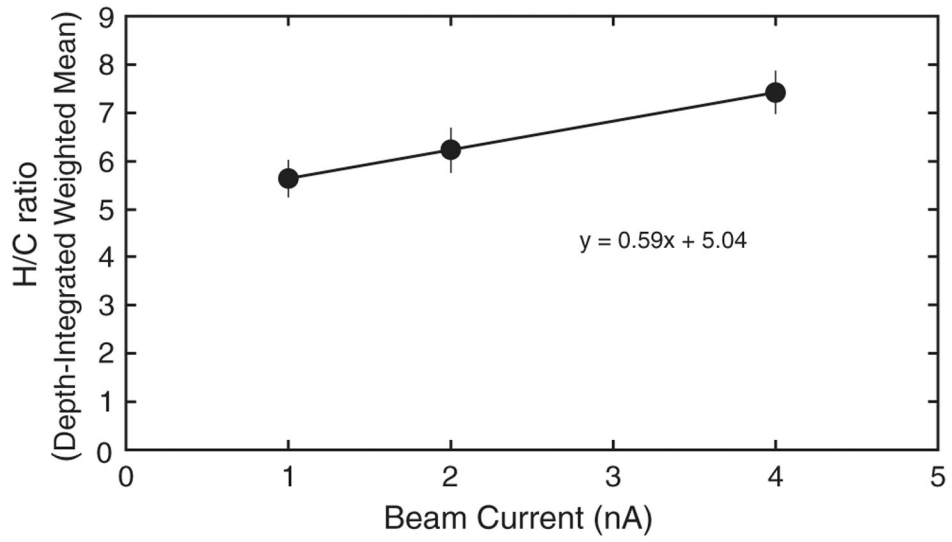

Fig. 3.

This diagram shows the effect of beam current on the final integrated H/C ratio. The ratio was calculated as the weighted mean of the measured $^{1}H/^{12}C$ and $^{12}C^{1}H/^{12}C_2$ ratios as described in the section on edge effects. The three points are each means of several measurements and the error bars are the 2-sigma SDs of the measurements. All measurements were made on the same standard under the same instrumental conditions, except that three different primary beam currents were used. The plotted values are integrated ratios measured on the same standard. Thus, the trend is not expected to go through zero. The trend indicates that hydrogen and carbon have different dependences on beam current. For each element, the ion yield does not increase proportionally with beam current, but the trend indicates that hydrogen count rate increases more rapidly with beam current than the carbon count rate.

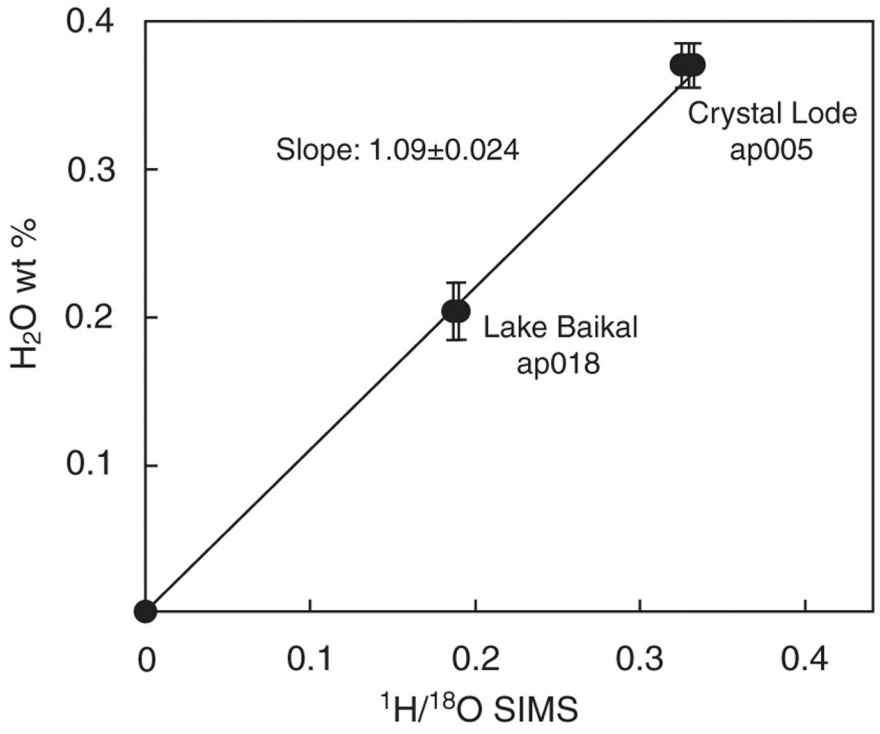

Fig. 4.

Plot of measured water contents (McCubbin et al. 2012) versus $^{1}H/^{18}O$ ratio for the two apatite standards used in this work. The measured data come from many spot analysis measured during a single session in the University of Hawai'i laboratory. The water content closely tracks the ion ratio, indicating that the hydrogen abundances for these two standards are accurate to ±2.4%.

Fig. 5.

Arrangement of samples and standards on the plate that was implanted with hydrogen for this work. The two apatite standards are in the round yellowish disk in the upper center. Three pieces of diamond-like carbon (dlc) on silicon (DOS) are the purple-colored pieces at the bottom center, left center, and top right. Flight samples are the small pieces circled in red just below center (B/C array) and at the right side (H array) of the plate. The plate is 3 × 3 inches across.

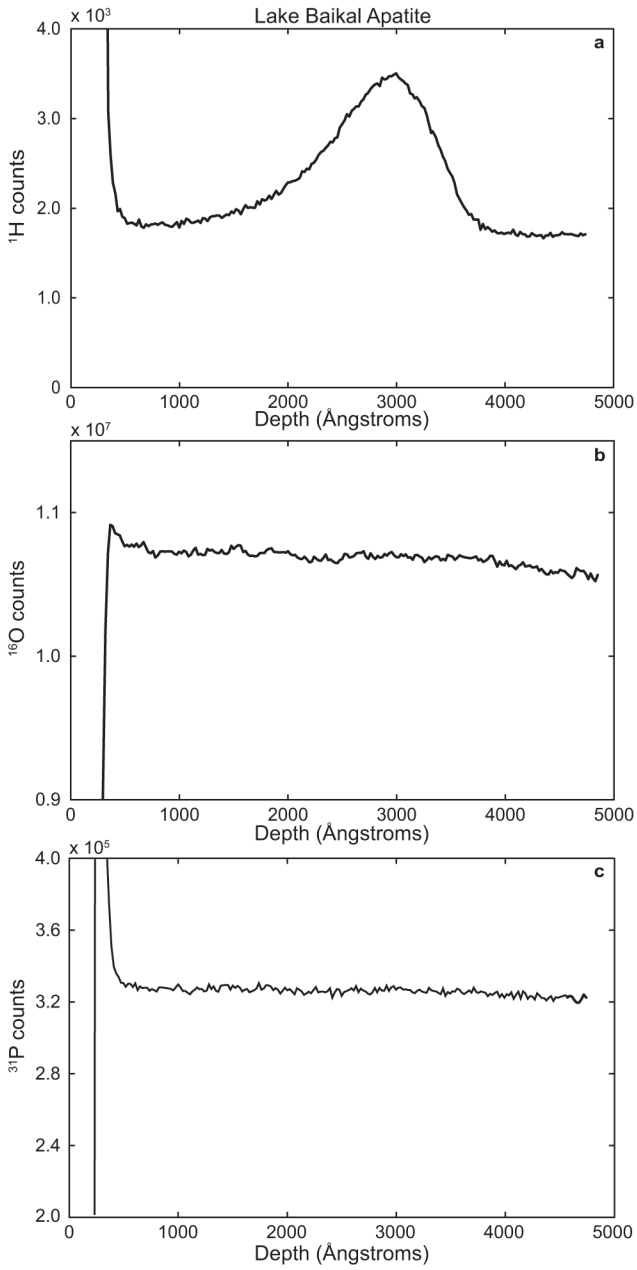

Fig. 6.

Count rate profiles for (a) ^{1}H, (b) ^{16}O, and (c) ^{31}P for a measurement of Lake Baikal apatite. The profiles do not extend to the surface because of presputtering. The ^{16}O and ^{31}P profiles show gentle decreases in count rate over the measurement, reflecting the slow decrease in primary beam current.

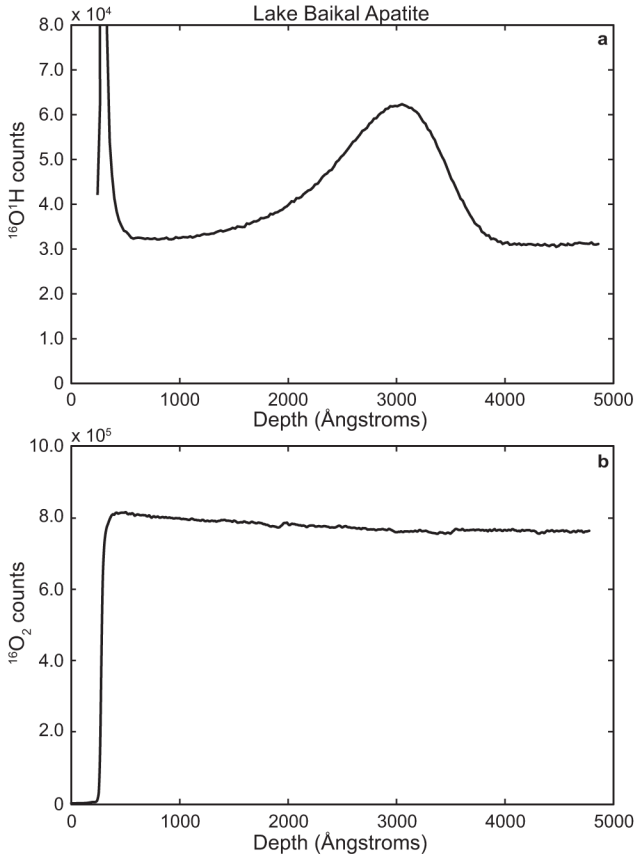

Fig. 7.

Count rate profiles for (a) $^{16}O^{1}H$ and (b) $^{16}O_2$ for a measurement of Lake Baikal apatite. The profiles do not extend to the surface because of presputtering. The $^{16}O_2$ count rate is decreasing slowly over the course of the measurement.

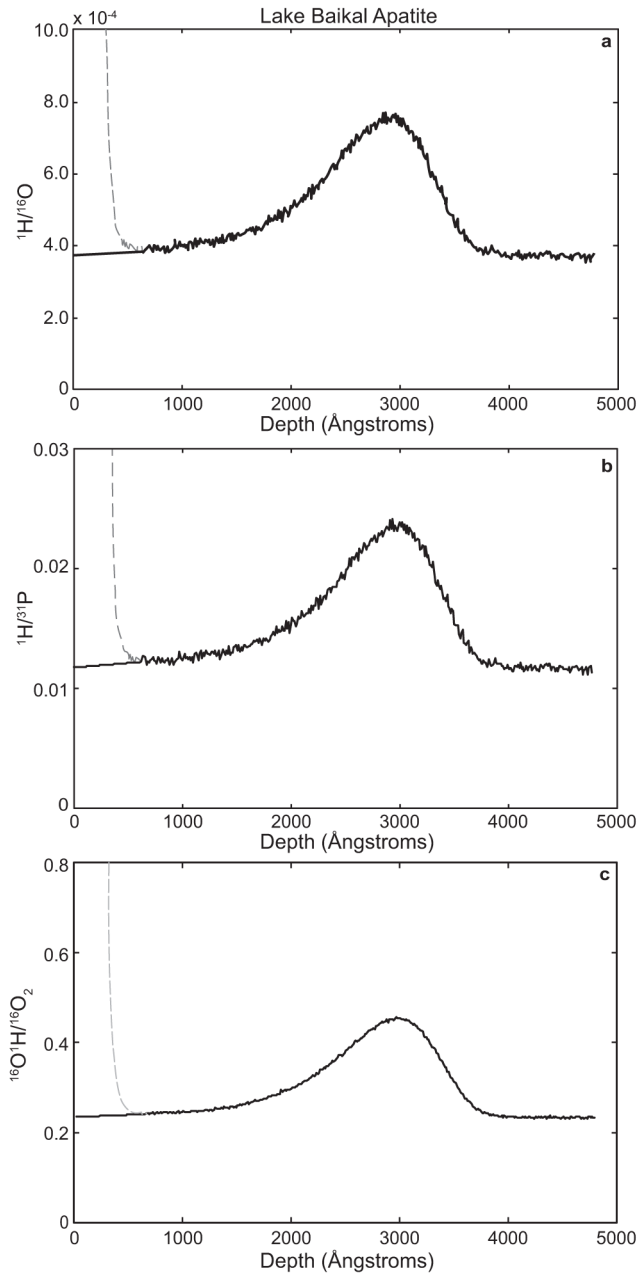

Fig. 8.

a) $^{1}H/^{16}O$ profile, b) $^{1}H/^{31}P$ profile, and c) $^{16}O^{1}H/^{16}O_{2}$ profile for the same Lake Baikal measurement shown in Figs. 6 and 7. The dashed lines are the measured ratios and are artifacts produced by surface hydrogen. To address this, we modeled the front ~450 Å by extrapolating the profiles to zero depth.

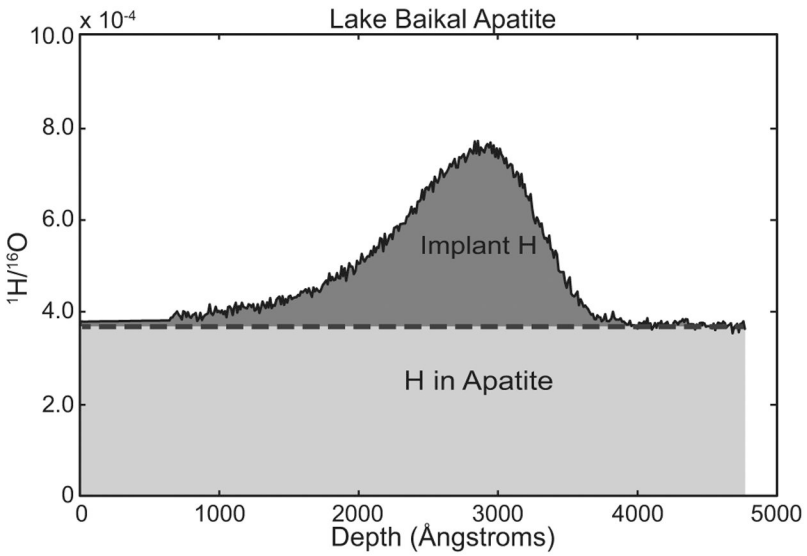

Fig. 9.

Depth profile of a measurement of the implanted H into Lake Baikal apatite. The lighter colored rectangle represents the integrated intrinsic $^{1}H/^{16}O$ profile. The darker shaded area under the ratio curve represents the integrated standard ^{1}H implant.

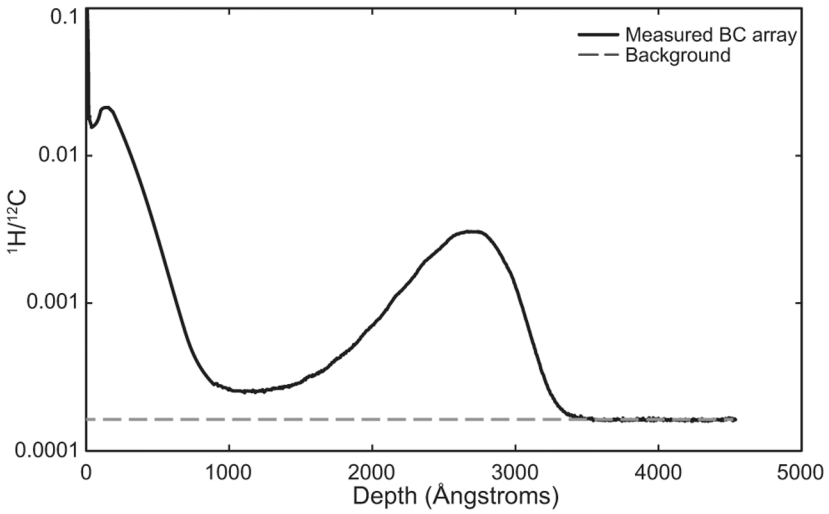

Fig. 10.

Depth profile of a measurement from the B/C array. The first curve is the solar wind profile and the second is the implanted standard. The dashed line represents the background in the collector chip. The solar wind and standard implant overlap at ~800–1500 Å and we must use templates to deconvolve the two profiles.

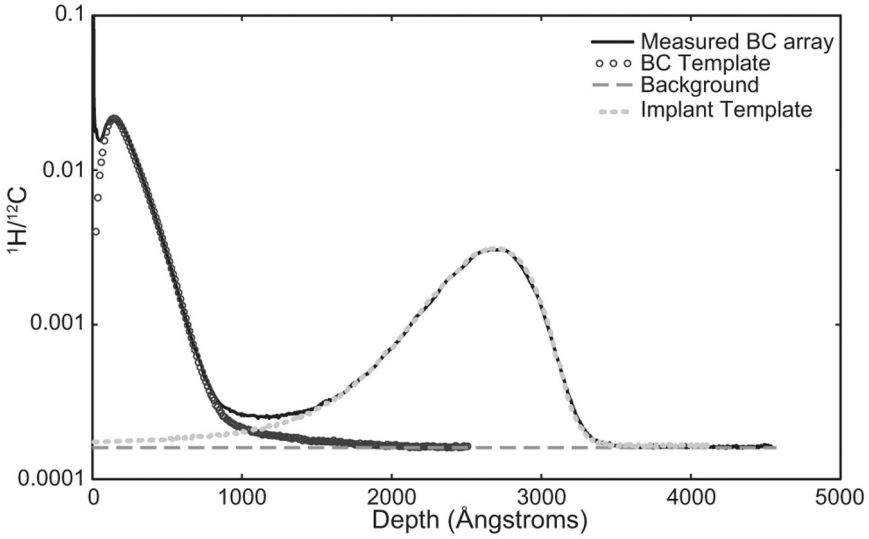

Fig. 11.

An example of the matched templates for one of our B/C measurements. The solid black line is the measured solar wind plus standard profile. The open circles represent the solar wind template (obtained from a measurement prior to implanting the standard into the sample; the shallow part of the solar wind template was estimated using SRIM). The gray short-dashed lines represent the standard template measured in a piece of flight-like DOS and the gray long-dashed line represents the constant background.

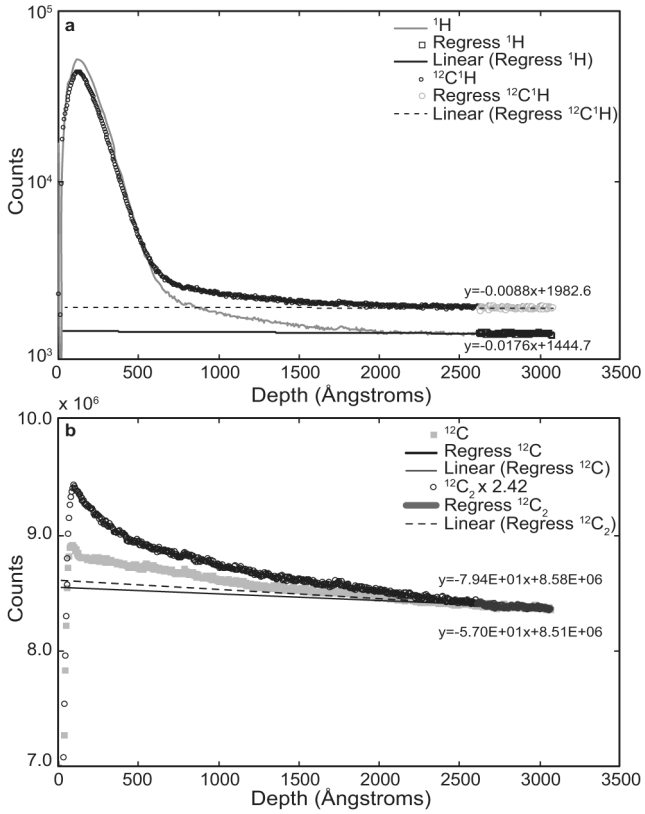

Fig. 12.

Measured counts as a function of depth for ^{1}H, ^{12}C^{1}H, ^{12}C, and ^{12}C$_2$ during a measurement of the Genesis E array. a) The ^{1}H counts are higher than the ^{12}C^{1}H counts in the solar wind peak, but the baseline counts are lower for ^{1}H than for ^{12}C^{1}H. The solid and dashed lines represent linear regressions through the deepest part of the profile. Note that the ^{1}H regression is decreasing more rapidly than the ^{12}C^{1}H profile near the end of the measurement. b) The counts of the matrix ions, ^{12}C and ^{12}C$_2$ decrease significantly over the course of the measurement (^{12}C, ~9%; ^{12}C$_2$, ~12%). Ratios calculated from ^{1}H and ^{12}C (higher numerator, lower denominator) will be higher than those calculated from ^{12}C^{1}H and ^{12}C$_2$ (higher numerator, lower denominator for the atomic ions). In addition, ratios calculated from the shallow part of the crater will be lower than those calculated from the deep part of the crater, with the biggest difference for the molecular ratios. Together, these behaviors explain why the fluences derived from the molecular ions are always lower than those derived from the atomic ratios.

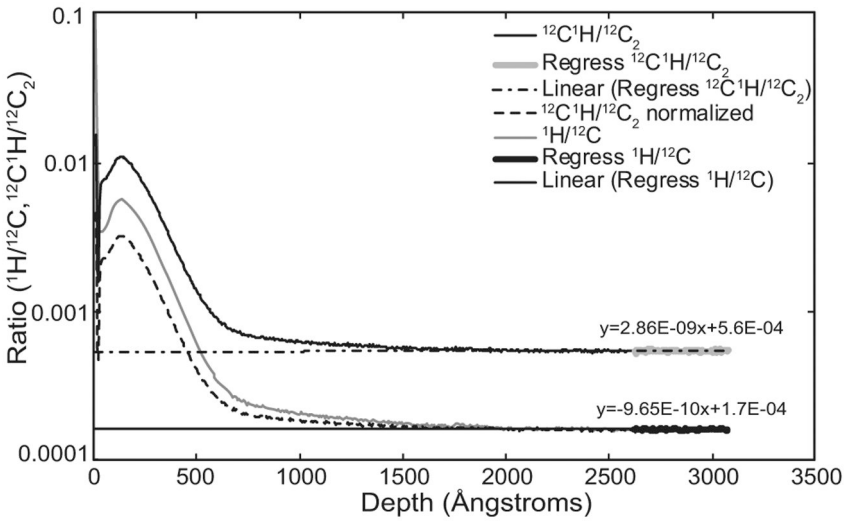

Fig. 13.

Ratios for $^1H/^{12}C$ (gray curve) and $^{12}C^1H/^{12}C_2$ (black curve) for the Genesis E-array data plotted in Fig. 12. To facilitate comparison, the $^{12}C^1H/^{12}C_2$ ratio (dashed curve) has also been scaled to the same background level as $^1H/^{12}C$. The peak for $^1H/^{12}C$ is significantly higher than that for $^{12}C^1H/^{12}C_2$. When standardized to an implant center peak at ~3000 Å, the atomic-ion data will give a higher fluence than the molecular-ion data.

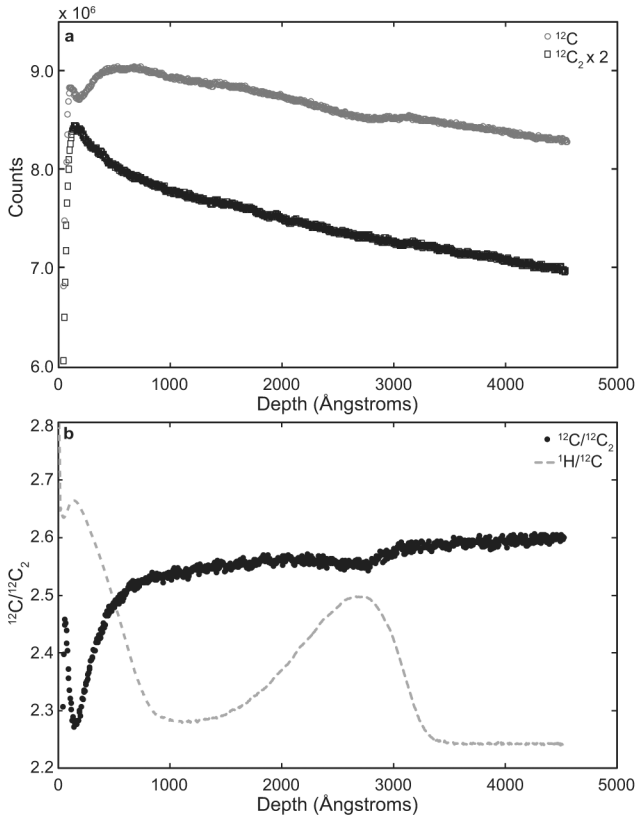

Fig. 14.

The count rates for ^{12}C and $^{12}C_2$ are shown for a B/C array measurement. b) $^{12}C/^{12}C_2$ is plotted to emphasize the difference in behavior for these two matrix ions. The measurement profile for $^{1}H/^{12}C$ is shown schematically for comparison. The dip in ^{12}C for the solar wind is accompanied by a higher $^{12}C_2$ count rate, making a strong feature in the $^{12}C/^{12}C_2$ plot. Note that both the solar wind and standard implants are accompanied by a dip in $^{12}C/^{12}C_2$.

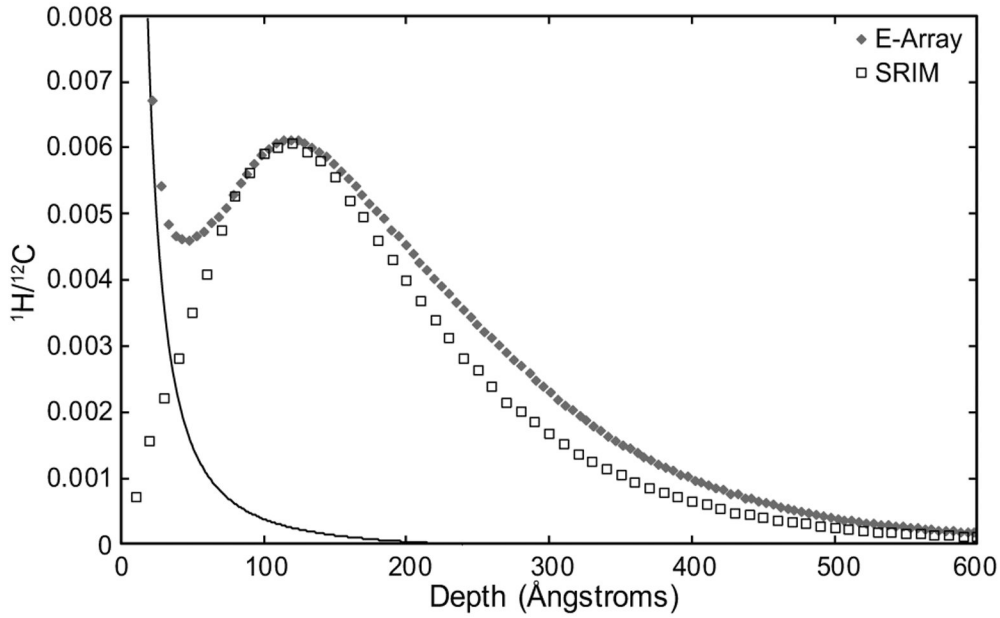

Fig. 15.

A measurement from the E array (solid diamonds) with a SRIM implant (open squares). To fix the front of the profile due to surface hydrogen and transient sputtering effects, the SRIM profile is used as a template for the first ~80 Å. The solid line shows a model for the gardened-in surface hydrogen.

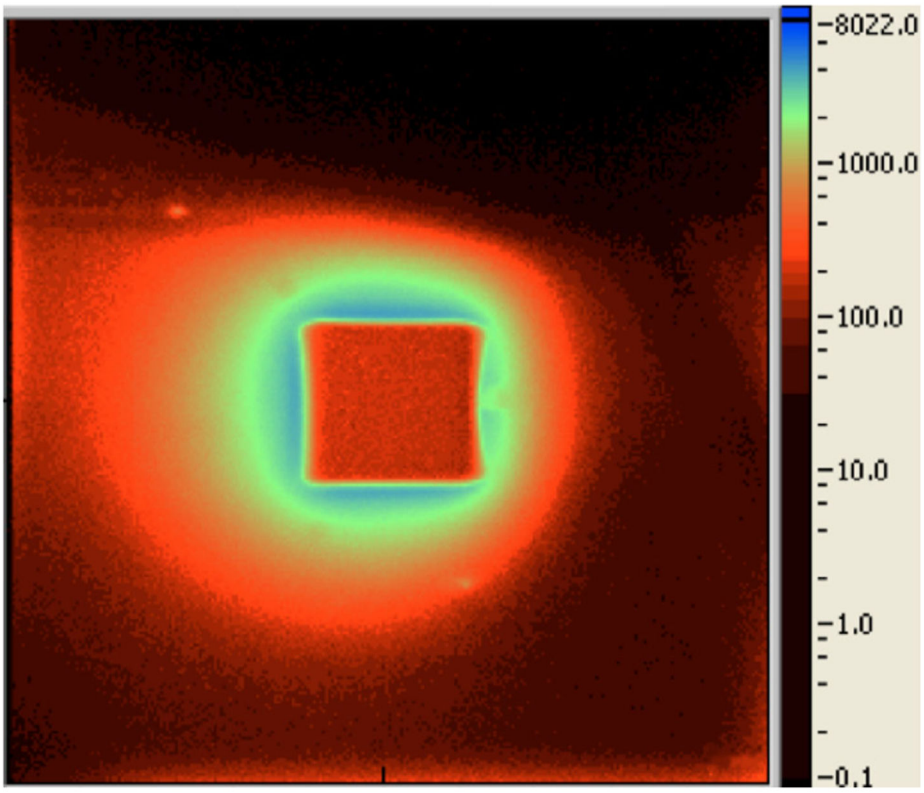

Fig. 16.

H^- ion image of a measurement crater in one of the Genesis collectors. The 50 × 50 μm^2 square in the middle is the footprint of the depth profile. The bright area around the crater is hydrogen that was sputtered from the crater and redeposited into the collector during the measurement. Hydrogen was also redeposited into the crater, where it was re-sputtered during the measurement (see text).

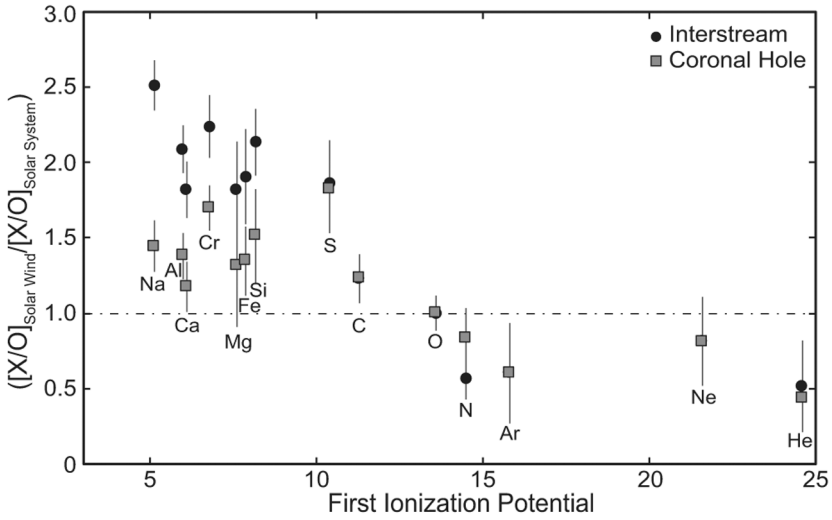

Fig. 17.

Element/oxygen ratios in two solar wind regimes are plotted normalized to the element/oxygen ratio in the photosphere as a function of first ionization potential. In the interstream solar wind, elements with low FIP are enriched in the solar wind relative to oxygen by factors of up to three, while high-FIP elements are either depleted or essentially unfractionated. Coronal hole wind shows a similar trend, but with significantly less fractionation. Solar wind data from Bochsler (2007a), solar system data from Asplund et al. (2009).

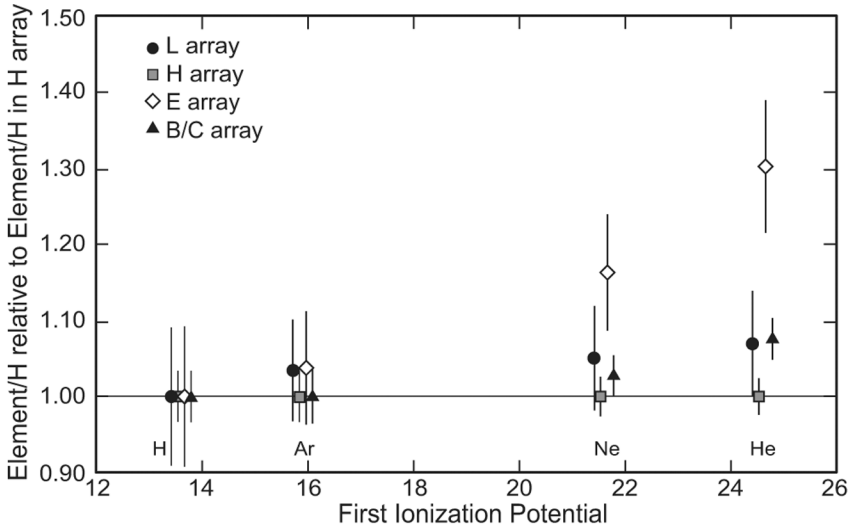

Fig. 18.

Solar wind argon, neon, and helium (from Heber et al. 2009a, 2012) are plotted as ratios to hydrogen (from this study) for the L array (interstream wind), E array (coronal mass ejections), and B/C (bulk solar wind). The data are normalized to the same ratios for the H array (coronal hole wind), because coronal hole wind is thought to be least effected by FIP fractionation. Coronal mass ejections show a smooth increase in ratios with increasing FIP, with the highest ratio for He, as is often observed in coronal mass ejections. The L array shows a more muted increase with increasing FIP.

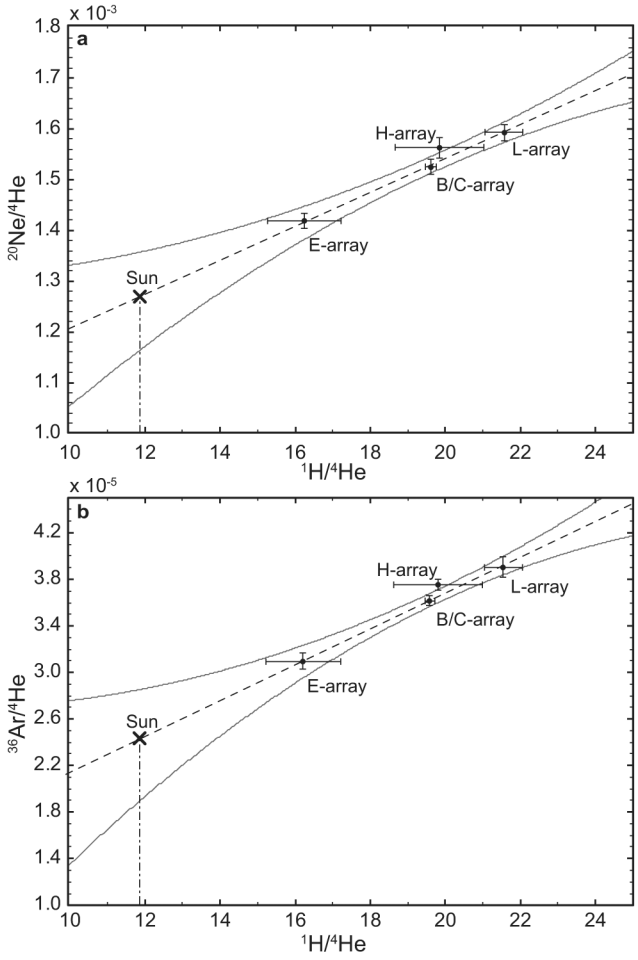

Fig. 19.

Solar wind noble gases and hydrogen determined from Genesis may provide good estimates of helium and argon in the Sun. a) Data for the four Genesis solar wind arrays are plotted on a $^{20}Ne/^{4}He$ versus $^{1}H/^{4}He$ plot. The data form a relatively tight array, which when regressed to the $^{1}H/^{4}He$ ratio in the Sun, give the $^{20}Ne/^{4}He$ ratio in the Sun, which in turn gives the solar neon abundance. b) A similar plot of $^{36}Ar/^{4}He$ versus $^{1}H/^{4}He$ also gives a relatively tight array, which can be used to determine the argon abundance in the Sun (see text).

Table 1.

Materials measured and their properties.

Sample	Sample #	Conductive	Hydrogen content known	Standard implanted
Lake Baikal apatite[a]		No	Yes	Yes
Crystal Lode apatite[a]		No	Yes	Yes
Flight-spare DOS chip[b]		Yes	No	Yes
Genesis B/C array chip	60628	Yes	No	Yes
Genesis H array chip	60631	Yes	No	Yes
Genesis L array chip	60431	Yes	No	No
Genesis E array chip	60625	Yes	No	No

[a]Natural sample used to calibrate hydrogen implant.

[b]DOS chip from Genesis preflight archive implanted with standard implant.

Table 2.

Fluence of ^{1}H standard implant ($\times 10^{15}$ H cm^{-2}).[a]

Measurement	$^{1}H/^{16}O$	$^{1}H/^{31}P$	$^{16}O^{1}H/^{16}O_2$
Crystal Lode #1	5.57	5.50	5.35
Crystal Lode #2	5.54	5.59	5.53
Mean Crystal Lode	5.56 ± 0.04[b]	5.55 ± 0.13[b]	5.44 ± 0.26[b]
Lake Baikal #1	5.88[c]	5.92[c]	5.13[c]
Lake Baikal #2	5.95	5.99	5.52
Lake Baikal #3	5.81	5.84	5.64
Mean Lake Baikal	5.88 ± 0.14[b]	5.92 ± 0.15[b]	5.43 ± 0.53[b]
Mean from atom ratios[d]	5.73 ± 0.41[e]		

[a] Nominal implant fluence 6×10^{15} H cm^{-2}.

[b] Uncertainties on mean values are 2σ SDs of the measurements. Statistical uncertainties are insignificant.

[c] Measured at 300 pAmps beam current; others were measured at 500 pAmps.

[d] Mean of results from atomic ratios (each standard and ratio given the same weight).

[e] Uncertainty does not include the uncertainty in the true water contents of the two apatites.

Table 3.

Hydrogen fluences calculated for B/C and H arrays (10^{16} atoms cm^{-2}).

From ratios	**B/C array**		**H array**	
Standard	**$^{1}H/^{12}C$**	**$^{12}C^{1}H/^{12}C_2$**	**$^{1}H/^{12}C$**	**$^{12}C^{1}H/^{12}C_2$**
Internal	1.634 ± 0.028	1.437 ± 0.052	0.551 ± 0.012	0.522 ± 0.010
External DOS	1.850 ± 0.098	1.642 ± 0.116	0.658 ± 0.016	0.593 ± 0.044
External B/C	—	—	0.582 ± 0.033	0.520 ± 0.053
External H	1.548 ± 0.074	1.446 ± 0.110	—	—
From cps/nA	**B/C Array**		**H Array**	
Standard	**^{1}H**	**$^{12}C^{1}H$**	**^{1}H**	**$^{12}C^{1}H$**
Internal	1.637 ± 0.028	1.548 ± 0.026	0.567 ± 0.016	0.557 ± 0.021
External DOS	1.695 ± 0.081	1.495 ± 0.033	0.711 ± 0.045	0.686 ± 0.032
External B/C	—	—	0.696 ± 0.033	0.722 ± 0.033
External H	1.376 ± 0.084	1.243 ± 0.032	—	—

Listed errors are 2σ SDs of measured values. A systematic error of ±5% from the uncertainty in the water contents of standard apatites should be quadratically combined with these values.

Fluences have been corrected for backscattered ions based on SRIM simulations (4% for B/C, 2.64% for H).

Table 4.

Fluences based on external standardization for L and E arrays (10^{16} atoms cm^{-2}).

From ratios	**L array**		**E Array**	
Standard	**$^{1}H/^{12}C$**	**$^{12}C^{1}H/^{12}C_2$**	**$^{1}H/^{12}C$**	**$^{12}C^{1}H/^{12}C_2$**
Flight-spare DOS	0.726 ± 0.016	0.886 ± 0.057	0.479 ± 0.015	0.436 ± 0.028
B/C implant	0.641 ± 0.036	0.776 ± 0.074	0.423 ± 0.026	0.382 ± 0.037
H implant	0.607 ± 0.011	0.780 ± 0.056	0.401 ± 0.012	0.384 ± 0.027
From cps/nA	**L array**		**E Array**	
Standard	**^{1}H**	**$^{12}C^{1}H$**	**^{1}H**	**$^{12}C^{1}H$**
Flight-spare DOS	0.684 ± 0.034	0.734 ± 0.015	0.423 ± 0.022	0.386 ± 0.011
B/C implant	0.669 ± 0.019	0.773 ± 0.017	0.414 ± 0.013	0.406 ± 0.012
H implant	0.556 ± 0.035	0.610 ± 0.014	0.343 ± 0.022	0.321 ± 0.009

Listed errors are 2σ SDs of measured values. A systematic error of ±5% from the uncertainty in the water contents of standard apatites should be quadratically combined with these values.

Fluences have been corrected for backscattered ions based on SRIM simulations (4.97% for L, 4.13% for E).

Table 5.

Hydrogen fluence in genesis collectors compared to results from the genesis ion monitor ($\times 10^{16}$ ^{1}H cm^{-2}).

Regime	Genesis ion monitor[a]	Genesis collectors	Ratio
BC array	2.06	1.634 ± 0.028[b]	0.79
L array	0.915	0.624 ± 0.043[b]	0.68
E array	0.473	0.412 ± 0.030[b]	0.87
H array	0.640	0.551 ± 0.012[b]	0.86
H+E+L	2.03	1.587 ± 0.045	
Diff. from B/C	1.5%	3.0%	

[a]Data from Reisenfeld et al. (2013), who give an uncertainty of ±20% (2σ) on the reported GIM values.

[b]Uncertainties are the 2σ SDs of the individual measurements. They do not include a ±5% systematic uncertainty from the H_2O contents of the apatite standards.